Distribution of oceanic crust in the Enderby Basin offshore East Antarctica

Tabea Altenbernd-Lang,[1] Wilfried Jokat [1,2] and German L. Leitchenkov [3,4]

[1]*Geophysics Department, Alfred Wegener Institute, Helmholtz Centre for Polar and Marine Research, Am Alten Hafen* 26, 27568 *Bremerhaven, Germany. E-mail: tabea.altenbernd@awi.de*

[2]*Geoscience Department, University of Bremen, Klagenfurter Str.* 4, 28359 *Bremen, Germany*

[3]*Department of Antarctic Geoscience, All-Russia Scientific Research Institute for Geology and Mineral Resources of the Ocean, Angliiskii pr.* 1, *St. Petersburg* 190121, *Russia*

[4]*Geology Department, Institute of Earth Sciences, Saint Petersburg State University, Universitetskaya nab.* 7-9, St. Petersburg 199034, *Russia*

SUMMARY

Seismic reflection and refraction data were collected in 2007 and 2012 to reveal the crustal fabric on a single long composite profile offshore Prydz Bay, East Antarctica. A *P*-wave velocity model provides insights on the crustal fabric, and a gravity-constrained density model is used to describe the crustal and mantle structure. The models show that a 230-km-wide continent–ocean transition separates stretched continental from oceanic crust along our profile. While the oceanic crust close to the continent–ocean boundary is just 3.5–5 km thick, its thickness increases northwards towards the Southern Kerguelen Plateau to 12 km. This change is accompanied by thickening of a lower crustal layer with high *P*-wave velocities of up to 7.5 km s^{-1}, marking intrusive rocks emplaced beneath the mid-ocean ridge under increasing influence of the Kerguelen plume. Joint interpretations of our crustal model, seismic reflection data and magnetic data sets constrain the age and extent of oceanic crust in the research area. Oceanic crust is shown to continue to around 160 km farther south than has been interpreted in previous data, with profound implications for plate kinematic models of the region. Finally, by combining our findings with a regional magnetic data compilation and regional seismic reflection data we propose a larger extent of oceanic crust in the Enderby Basin than previously known.

Key words: Composition and structure of the oceanic crust; Antarctica; Crustal structure.

1 INTRODUCTION

The geometries and distributions of the present-day southern continents and oceanic basins are products of the breakup and dispersal of Gondwana since the Jurassic. The detachment of continents from Antarctica (ANT) continued for more than 100 Myrs after starting between Antarctica and Africa (AFR) about 165 Ma with the formation of the oceanic Riiser Larsen Sea/Mozambique Basin (Jokat *et al.* 2003; König & Jokat 2010; Leinweber & Jokat 2012; Mueller & Jokat 2019). This separation was accompanied by massive volcanism both onshore Africa–Antarctica as well as in the newly formed oceanic basins. During the separation of Antarctica and Africa, India and Madagascar still were parts of the Antarctic Plate. This plate further fragmented around 133 Ma, leading to the separation of India–Madagascar from Antarctica to form oceanic basins in the Bay of Bengal and Enderby Basin.

During the early part of this drift phase, the dispersal was accompanied by excess magmatism related to the arrival of the Kerguelen mantle plume. Remnants of volcanism from this event are known onshore in the Prydz Bay region, from the western flank of the Lambert Rift (Coffin *et al.* 2002; Sushchevskaya *et al.* 2018), and from the Rajmahal flood basalts erupted onshore between 112 and 118 Ma in the conjugate parts of India (e.g. Mahoney *et al.* 1983; Kent *et al.* 2002). Offshore, plume-related magmatism formed the Kerguelen Plateau (KP, Fig. 1), the second-largest large igneous province (LIP) preserved anywhere on Earth. The KP erupted during several magmatic phases from south to north, as documented by eleven ODP drill sites (Frey *et al.* 2003). Important for our study are two results, which played an important role for any recent kinematic model for the Antarctic–Indian breakup. First, the oldest basalts drilled at the southern Kerguelen Plateau (SKP) have an age of 121 Ma, at site 1136 (Jiang *et al.* 2021) Geochemical analyses indicate that the SKP basalts from sites 738, 749, 750 and 1137 solidified from melts that contained small components (<5–7 per cent) of continental lithospheric origin (Fig. 1; Mahoney *et al.* 1995; Frey *et al.* 2000, 2002; Weis *et al.* 2001; Ingle *et al.* 2002). Secondly,
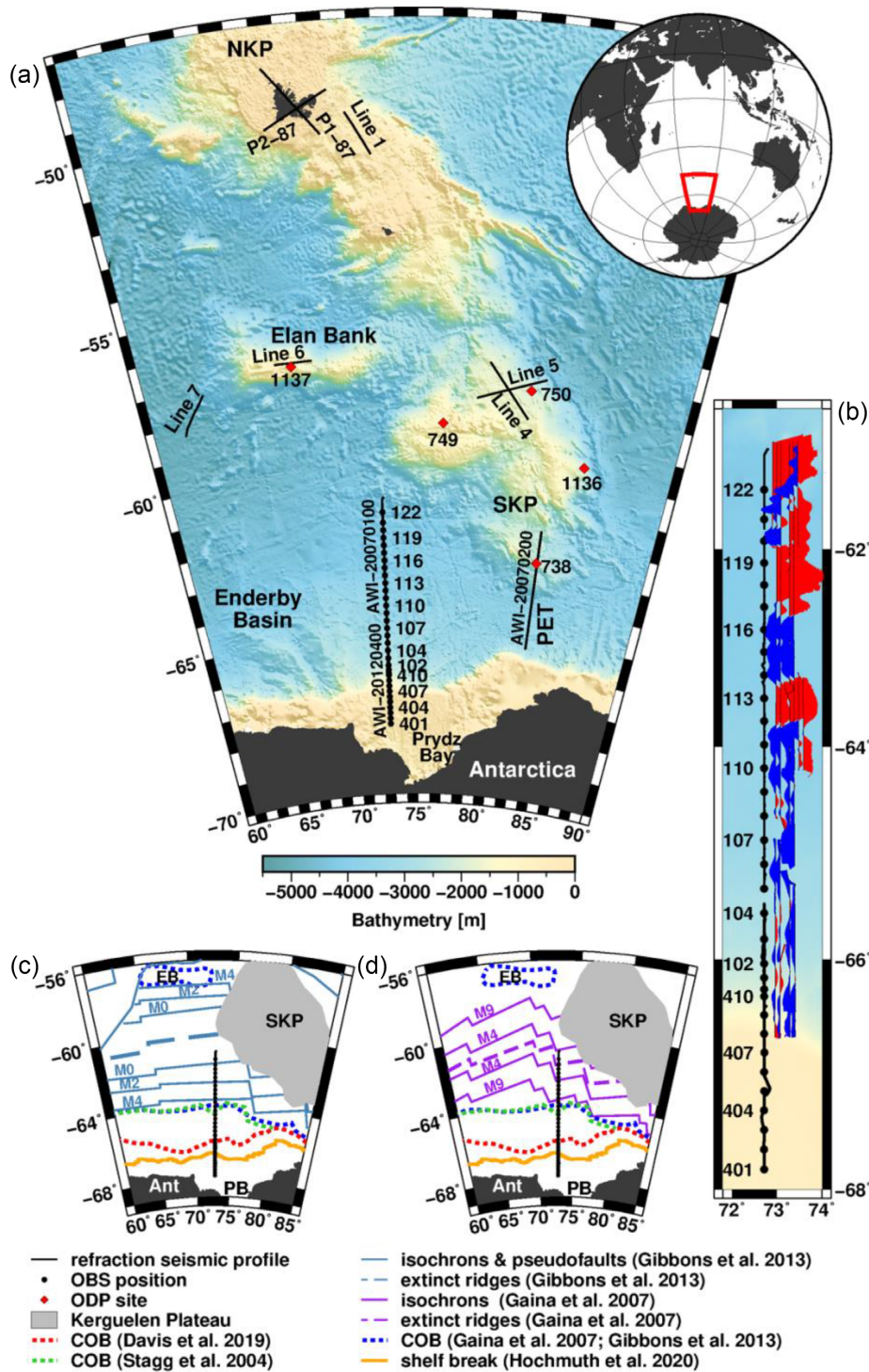
Figure 1. Overview maps. (a) Bathymetric map of the area of interest (GEBCO Bathymetric Compilation Group 2021). Black numbers indicate the OBS numbers along both profiles. (b) Helicopter borne magnetic data acquired along the profiles. The location of the magnetic profiles has been shifted to the right to aid visibility of the seismic profile. Panels (c) and (d) show the positions of different COBs, extinct ridges and isochrons. Abbreviations: Ant, Antarctica; COB, continent–ocean boundary; EB, Elan Bank; PB, Prydz Bay; PET, Princess Elizabeth Trough; NKP, Northern Kerguelen Plateau; SKP, Southern Kerguelen Plateau.

coring at Site 1137, located to the northwest on Elan Bank (Fig. 1), returned clasts of garnet-biotite gneiss from a fluvial conglomerate intercalated with basalts (Frey *et al.* 2000). Analyses of the clasts revealed similarities to gneisses known from eastern India and East Antarctica (Frey *et al.* 2003). Most of these studies concluded that the continental-related volcanism occurred close to the drill sites and that Elan Bank and parts of the SKP may therefore be isolated microcontinents.

1.2 Kinematic models

The age information from ODP/IODP expeditions together with regional magnetic data sets along the East Antarctic and East Indian rifted margins form the basis for a range of plate kinematic models describing the breakup and subsequent drift of India and Madagascar away from Antarctica. The lack of high quality deep seismic data off East India and East Antarctica as well as widely spaced magnetic data along the conjugate continental margins hinder a robust identification of the structural elements (continent–ocean transition zone, onset of oceanic crust and spreading anomalies). Because of these large spatial uncertainties, several different interpretations of the magnetic chrons exist, causing contrasting kinematic models for the evolution of the conjugate margins off East India–Antarctica. Interpretations of the widely spaced and noisy magnetic anomaly profiles in the Bay of Bengal and Enderby Basin rely heavily on the locations of their continent–ocean boundaries (COBs), at the onset of oceanic crust. Identifying the COB unequivocally is, however, difficult to do in the absence of deep seismic data; existing interpretations for the COB disagree in location by as much as 400 km in the Enderby Basin, and 430 km in the Bay of Bengal (Eagles *et al.* 2015). This sustains multiple interpretations of magnetic reversal isochrons, particularly in the Enderby Basin, where many studies require an extinct spreading axis to explain the isolation of microcontinental blocks beneath the SKP and Elan Bank (Figs 1c and d).

Broadly, the conflicting sets of interpretations fall into one of two classes. In the first, the lack of strong correlations between magnetic profiles is taken to indicate that the ocean crust formed partially or wholly during the magnetic Cretaceous Normal Superchron (CNS, 120–84 Ma, Royer & Coffin 1992; Banerjee *et al.* 1995; Jokat *et al.* 2010). In the second, weak correlations are proposed off east India, Sri Lanka, and in the Enderby Basin, to be interpretable in terms of weak M-series isochrons in oceanic crust that formed between 134 and 130 Ma (e.g. Ramana *et al.* 1994, 2001; Nogi *et al.* 1996; Ishihara *et al.* 1999; Desa *et al.* 2006; Gaina *et al.* 2007; Gibbons *et al.* 2013).

By adding results from scientific drilling of the Kerguelen Plateau, new plate kinematic models no longer interpreted the east India and Antarctic margins as conjugate rifted margins. Critical for these new models were the drilled gneiss conglomerate on Elan Bank and the continental contaminated volcanic rocks from the SKP. These constraints led to two different scenarios for the Indian drift. The first class of interpretations (Royer & Coffin 1992; Banerjee *et al.* 1995; Ramana *et al.* 2001; Jokat *et al.* 2010) were used to support kinematic models in which the boundary between the Indian and Antarctic plates moved more or less continuously northwards since its formation close to the start of the CNS. The second class favoured an earlier initiation at 134 Ma (chron M11, Desa *et al.* 2006; Gaina *et al.* 2007), and suggested that whilst the boundary remained stable in the western Enderby Basin, farther east it jumped from south of Elan Bank and the SKP to north of them, detaching both microcontinents from the Indian Plate. An extinct spreading axis in the northern part of the Enderby Basin was introduced between the two microcontinents (Elan Bank and the SKP) and their conjugate continental margin of East Antarctica. According to these models, the jump saw seafloor spreading terminate in the eastern Enderby Basin between chrons M2 and M0 and re-establish in the eastern Bay of Bengal early in the CNS (124−84 Ma, Gaina *et al.* 2007). Subsequent models by Gibbons *et al.* (2013) and Talwani *et al.* (2016) modified these ideas (Fig. 1) by incorporating new interpretations of geophysical data off Antarctica and East India.

These modifications saw the extinct axis in the Enderby Basin shifted to the north and dated to 115 Ma, and the prominent Mac Robertson magnetic anomaly (MCA) reinterpreted as the M4 spreading isochron just north of a COB that formed during a westward-propagating continental breakup episode.

Jokat *et al.* (2010) acquired dense offshore aeromagnetic data in the western Enderby Basin to test for the presence of M-series isochrons required by the two-phase models. After finding no correlating reversal magnetic anomalies, they argued that seafloor spreading started forming the western Enderby Basin no earlier than the CNS (124–84 Ma). Gibbons *et al.* (2013) could not incorporate these results into their model without the implication of convergent plate motions for which there is no geological evidence. Since then, new seismic and magnetic observations have been made to support the formation of oceanic crust in two parts of the eastern Enderby Basin, off Prydz Bay and in the Princess Elizabeth Trough at chron M9r (Jokat *et al.* 2021). The authors found no evidence for an extinct spreading axis in the eastern Enderby Basin, and so concluded that the separation of India and Sri Lanka from Antarctica took place without major rift jumps as previously modelled by Royer & Coffin (1992) and Ramana *et al.* (2001). However, to accommodate contrasting spreading velocities in Prydz Bay and the Princess Elizabeth Trough, Jokat *et al.* (2021) had to introduce intracontinental movements within the Indian and/or Antarctic plates.

One of the new model constraints from Jokat *et al.* (2021) was the location of the COB in Prydz Bay. This COB is determined by using the deep seismic data that we present here in greater detail and with coincident gravity modelling and seismic reflection profiles. With the added confidence of these constraints, we extrapolate (i) COB identification throughout a regional network of multichannel seismic reflection profiles and (ii) magnetic isochron identifications throughout the existing network of magnetic anomaly profiles in the Enderby Basin. We discuss the implications of the resulting distribution of oceanic crust to the region's various previous plate kinematic models.

2 METHODS AND MODELLING

2.1 Seismic data acquisition

Seismic refraction data were acquired using ocean-bottom seismometers (OBS) and ocean-bottom hydrophones (OBH) along two seismic lines (Hubberten 2008, Fig. 1) during two expeditions in 2007 and 2012. The two experiments acquired coincident multichannel seismic (MCS) data (Figs 2 and 3) along a meridian at ~72°40′E.

The northern part of the two profiles, AWI-20070100, was acquired in 2007 during a joint expedition of the research vessels *Akademik Alexandr Karpinskiy* (RV *Karspinskiy*) and RV *Polarstern*. Difficult seasonal sea ice conditions prevented prolongation of this 625-km-long profile over the continental shelf in Prydz Bay to image the COB and the continent–ocean transition (COT) zone to the south. In total, 22 stations consisting of 3 OBH (stations 101–103) and 19 OBS (stations 104–122) were deployed at spacings ranging between 25 and 30 km for the acquisition of seismic refraction data. Two different seismic sources were used for seismic refraction data acquisition: on RV *Polarstern* an array of up to 8 G.Guns™ with a total volume of 68.2 l; on RV *Karpinskiy* two airguns with a total volume of 80 l. The shot interval was 60 s. During repair breaks of the G.Gun™ cluster of RV *Polarstern*, RV *Karpinskiy* provided the seismic source in order to avoid large shot
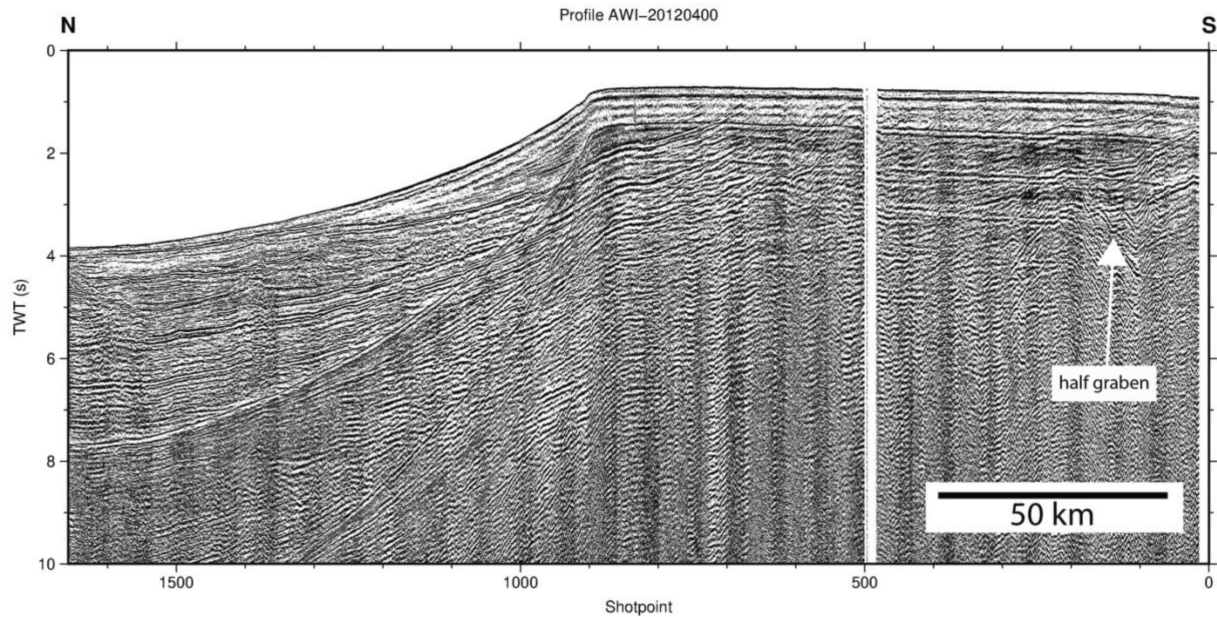
Figure 2. Seismic reflection data coincident with the deep seismic sounding line AWI-20120400. The quality of the MCS data along the profile is partly poor. The position of a half graben is labelled.
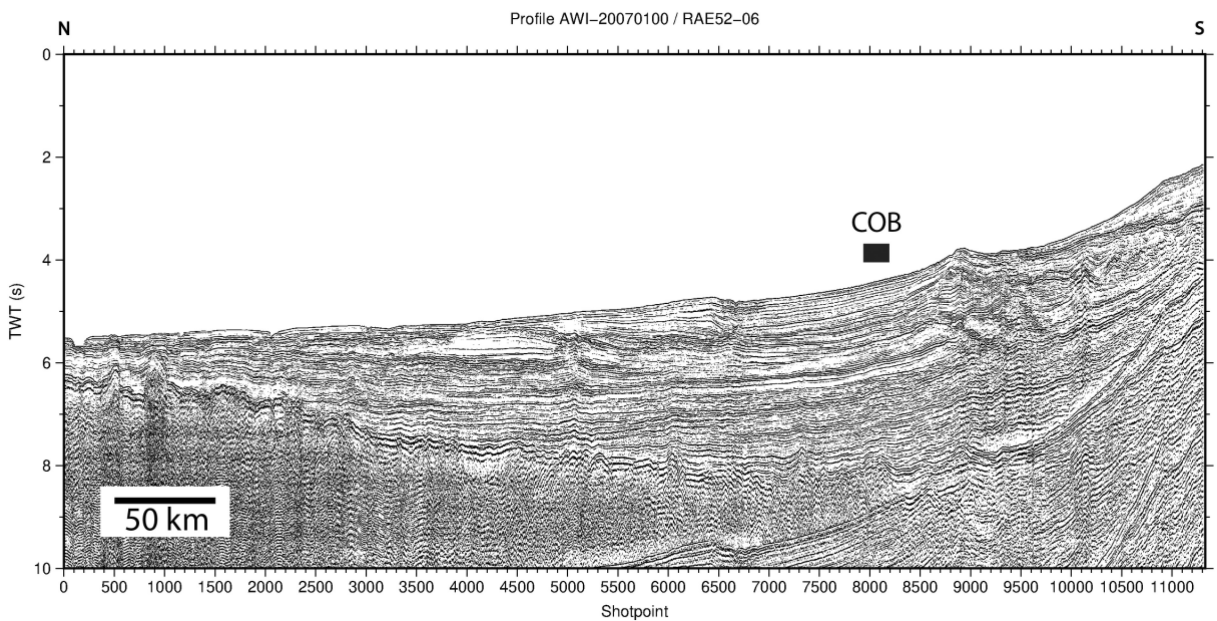
Figure 3. Deep-sea part of the seismic reflection data coincident with the deep seismic sounding line AWI-20070100. The position of the COB, derived from our *P*-wave velocity model, is labelled.

gaps. For MCS data acquisition, RV *Karpinskiy* towed a 4400-m-long streamer with 352 channels, recording arrivals with a sample rate of 2 ms and a recording length of 13 s. The seismic source for the MCS data acquisition consisted of 18 airguns with a total volume of 46 l.

RV *Karpinskiy* acquired additional geophysical data in 2012 in order to prolong the existing profile AWI-20070100 onto the shelf off Prydz Bay. The prolongation, AWI-20120400, partly overlaps line AWI-20070100 (Figs 1a and b) and extends a further ∼150 km onto the shelf, with 12 OBS stations deployed at an average distance

of ∼19 km. As in 2007, sea ice conditions and problems with the seismic source interrupted the seismic data acquisition several times, necessitating two different seismic sources to be used. The northern part of the refraction profile used an airgun array consisting of 18 sleeve guns with a volume of 30–47 l. Two airguns with a total volume of 60 l were operated for the southern part and the subsequent MCS data acquisition. A shot interval of 60 s was chosen to acquire the refraction and MCS seismic data. RV *Karpinskiy* deployed its 4400-km-long seismic streamer parallel to this line and recorded MCS data with the same settings as in 2007.

The sampling frequency was set to 250 Hz for all OBS systems used in 2007 and 2012. The OBS gain was set to 16 for the hydrophone channel and to 4 for the seismometer channels. The gain for the three OBH hydrophone channels was set to 5. The internal clocks of the recorders were synchronized with GPS time before deployment of all OBS and OBH systems. After recovery, the internal clocks were again synchronized to determine their drifts (skews). The data and log files were archived, processed, demultiplexed and finally stored in segy-format. The exact coordinates of the instrument positions at the seafloor are unknown since the instruments drift away from their deployment position while sinking to the seafloor. As a result, the direct wave in the seismograms can be asymmetric. To correct for this inaccuracy, the positions of the instruments were recalculated based on traveltime picks of the direct wave.

We complemented the MCS data using previously acquired profiles from two Russian Antarctic Expeditions (RAE-40, RAE-45, RAE-46, Gandyukhin *et al.* 2002; Leitchenkov *et al.* 2015) west of our deep seismic line. The Russian seismic data are available via the Antarctic Seismic Data Library System for Cooperative Research (SDLS).

2.2 Data quality and modelling of wide-angle data

The data quality of the OBS/OBH seismograms ranges from very good to poor. Examples are shown in Figs 4–9. Most seismometer components were quite noisy along profile AWI-20070100. Depending on the data quality, we used the hydrophone channel (stations 101–117, 120–121, 403, 409, 411) or the z-component of the seismometers (stations 118, 122, 401–402, 405–408, 410) for picking. OBS 404 did not record any useful data and OBS 119 could not be recovered. The software *ZP* (developed by Barry Zelt, see http://www.soest.hawaii.edu/users/bzelt) was used for phase picking. To enable accurate phase determination, the seismograms were bandpass filtered at 4–15 Hz for offsets of 20 km and at 4–12 Hz for longer offsets. Most seismic records of the northern and central OBS stations (OBS 108–122) are characterized by a high signal to noise ratio, which allow for the identification of seismic phases down to the upper crust and partly also the mantle. The higher noise levels in the records acquired south of station 108 makes the identification and picking of first arrivals more difficult.

Based on velocities, amplitude and curvature, we distinguished between refracted and reflected phases and picked the first arrivals. Refracted phases within the sedimentary layers (P_{sed1} to P_{sed5}) were identified in almost all seismic records, except at the northern end of the model where the sediment cover is partly less than 1.5 km thick (Fig. 4). Landwards, the thickness of the sediments increases, while the amplitudes especially of refracted arrivals within the lowermost sedimentary layer (P_{sed5}) decrease significantly, indicating a small impedance contrast (Fig. 5). Reflections at the base of sedimentary layers ($P_{sed1}P$ to $P_{sed5}P$) and intracrustal reflections ($P_{c1}P$ to $P_{c4}P$) are observed in all parts of the model (Figs 4–8), subdividing the sediments in up to five and the crust into two to four layers. Refracted arrivals within the crustal layers (P_{c1} to P_{c5}) could mainly be identified in the sections seaward of the shelf due to the noisy data in this area. The crustal refractions are characterized by velocities of 5.1–7.5 km s^{-1}. Undulations in the traveltimes of refracted and reflected crustal phases are for example related to half grabens (Fig. 2) at the landward end of the profile (Fig. 8, $P_{c3}P$) or a rough basement topography (e.g. Fig. 4, P_{c3} and P_{c4}). The high-amplitude

phase characterized by a slight curvature which is aligned approximately horizontal when plotted with a reduction velocity of 8 km s^{-1} was identified as reflection (P_mP) at the boundary between crust and mantle (Moho). Refracted arrivals from the upper mantle (P_n) with velocities of approximately 7.9 km s^{-1} have only been observed in some sections in the central part of the model (OBSs 107–109, 111), where the crust is fairly thin.

The 2-D velocity–depth model for the 770-km-long composite profile AWI-20070100/20120400 (Fig. 10) was produced using the graphical user interface *PRay* (Fromm 2016) for Zelt & Smith's (1992) software *rayinvr*. The upper part of our *P*-wave velocity model is constrained by bathymetry data and sediment and basement layer boundaries identified in the coincident MCS data (Figs 2 and 3). The MCS constraints were mostly excellent, except on the shelf where a strong water bottom multiple, typical for glaciated high latitudes shelves, allowed only limited insights into the deeper structure of the continental shelf. Based on the identified and picked reflected and refracted phases described above, we subdivided the model into five sedimentary layers (s1–s5), four crustal layers (c1–c4), and one mantle layer (Fig. 10).

In our description we refer to along-profile distances using terms like 'km 30′ in order to avoid misunderstandings with references to lengths or separations. Therefore, 'km 30′ should be understood as 'profile kilometre 30 from the beginning of the line'.

2.3 Uncertainties and errors

In general, the model is very well constrained by refractions and reflections in its northern and central parts, while the quality of the data is somewhat poor for the Prydz Bay shelf area (Fig. 10c). Reasons for the poor quality and ray coverage in some parts of the profile are noisy data and technical problems during the data acquisition. Numerous experiments conducted by AWI show that, in most cases, the use of an airgun array with a total volume of 60 l is sufficient to generate reasonable seismic signals for investigating the crustal fabric. However, this seems to be the lower limit of sound energy needed for such experiments. During the expedition in 2012, smaller airguns with a volume less than 60 l were partly used. It is likely that their volume was insufficient and their frequency not low enough to illuminate the deeper structures below the shelf. In addition, the MCS data indicate a complex shallow shelf geology (Fig. 2; half graben), which might have also contributed to the poor data quality at several stations by scattering seismic energy.

During the acquisition of profile AWI-20070100, problems with the seismic source caused several shot gaps (e. g. at km 95–105 and 485–510, Figs 4, 6 and 11). Despite these problems, enough stations provided sufficient data quality to achieve a reasonable velocity–depth model covering the COB. The ray coverage (Figs 10c and 12) is good to very good in the central part of the transect and also very good in the upper, sedimentary layers of the southern part. In contrast, the ray coverage south of km 500, especially in the lower crustal layers, is locally very sparse.

The *rayinvr* program provides an estimate on the statistical quality of the seismic velocity models using the normalized χ^2 method and the residual time tRMS (Zelt & Smith 1992). tRMS refers to the root mean square misfit between modelled and observed traveltimes. Error estimates for the traveltime picks were assigned and increase with the average depth of each layer, ranging between 0.045 and 0.1 s (Table 1, Fig. 11). Ideally, both the pick uncertainties and the tRMS misfit should be very small; the final model's tRMS is 0.059 s (Table 1). χ^2 weights the misfits between the picked phases in the
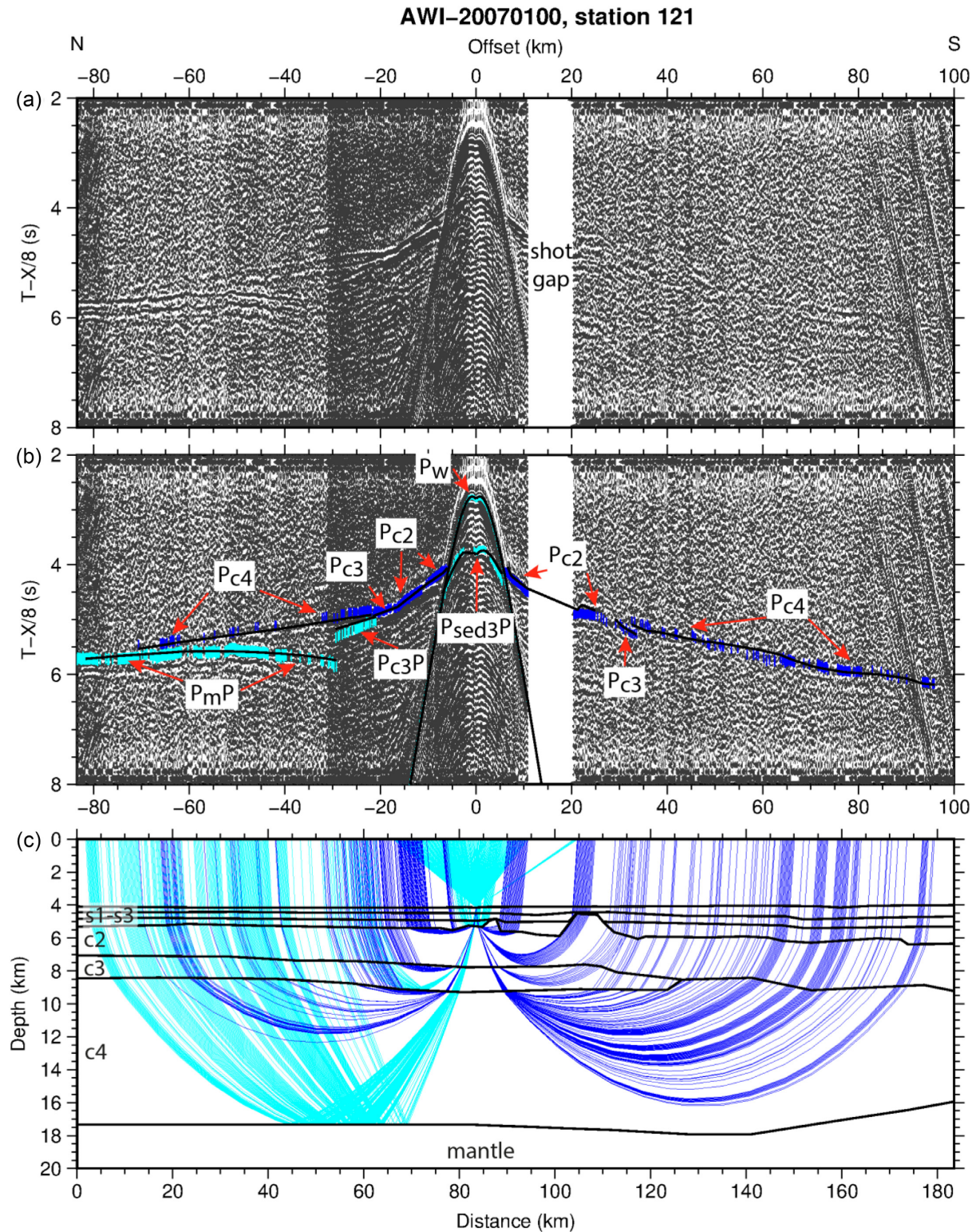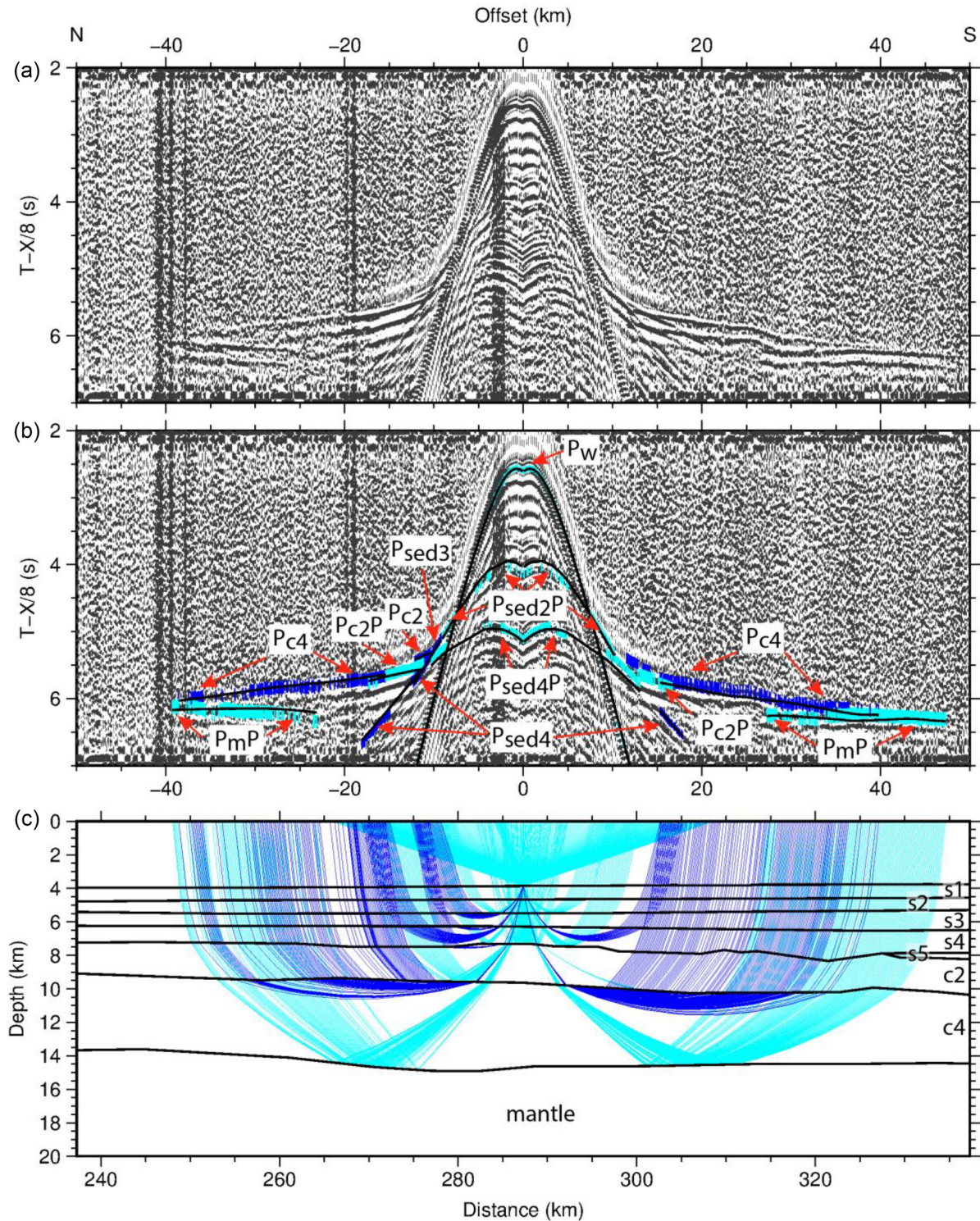
Figure 4. Picked and computed traveltimes of OBS 121 (changed after Jokat *et al.* 2021). (a) Seismic record section of the hydrophone (h) component. (b) Same section, picked phases are shown in dark blue (refractions) and light blue (reflections). The computed traveltimes are shown as black lines, phase names are labelled. (c) Ray paths of the picked phases shown above (Jokat *et al.* 2021). Black lines mark the layer boundaries of the velocity layers. Sedimentary layers (s1–s3), crustal layers (c2–c4) and the mantle are labelled.

seismograms and the modelled phases of the calculated traveltimes. $\chi^2 = 1.0$ denotes a perfect fit between the observed and calculated traveltimes (Zelt & Smith 1992). $\chi^2 > 1.0$ indicates that the error is underestimated and $\chi^2 < 1.0$ that the resolution of the model is too low to give a good certainty, therefore the error was overestimated. The χ^2 is 0.808 for our model, acceptably close to the ideal value of 1. Thus, picked and computed traveltimes correlate well (Fig. 11).
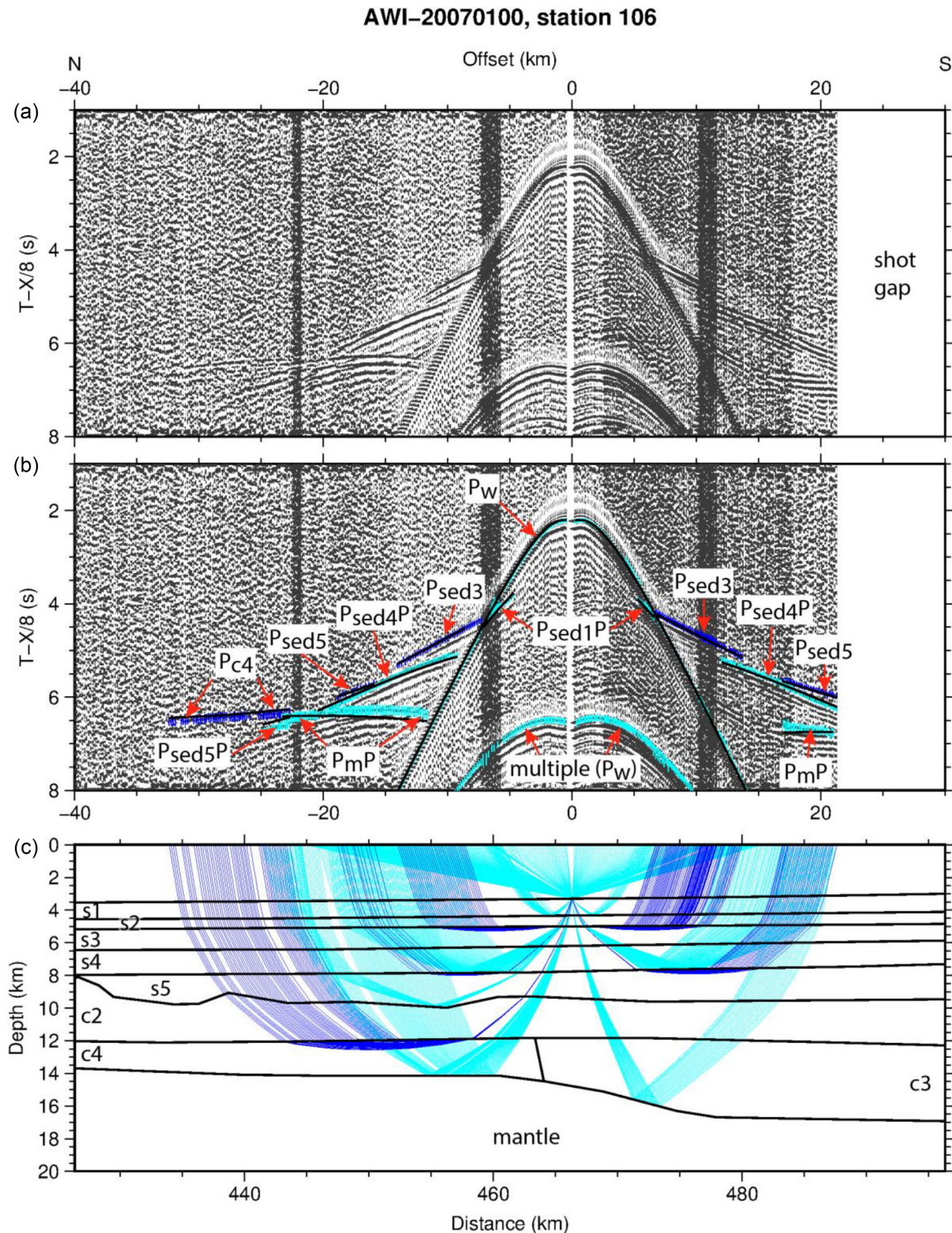
AWI–20070100, station 113

Figure 5. Picked and computed traveltimes of OBS 113. (a) Seismic record section of the hydrophone (h) component. (b) Same section, picked phases are shown in dark blue (refractions) and light blue (reflections). The computed traveltimes are shown as black lines, phase names are labelled. (c) Ray paths of the picked phases shown above. Black lines mark the layer boundaries of the velocity layers. Sedimentary layers (s1–s5), crustal layers (c2, c4) and the mantle are labelled.

The velocity resolution shown in Fig. 10(d) illustrates the diagonal values of the resolution matrix for the velocity nodes. Nodes with values >0.5 are considered to be well resolved (Lutter & Nowack 1990). In general, the sediment layers and large areas of the crustal layers north of km 470 are well resolved. Regions with poor resolution often coincide with regions of poor ray coverage, for example the crustal layers south of km 470, or wide areas of the mantle (Figs 10c and d). However, the resolution is highly
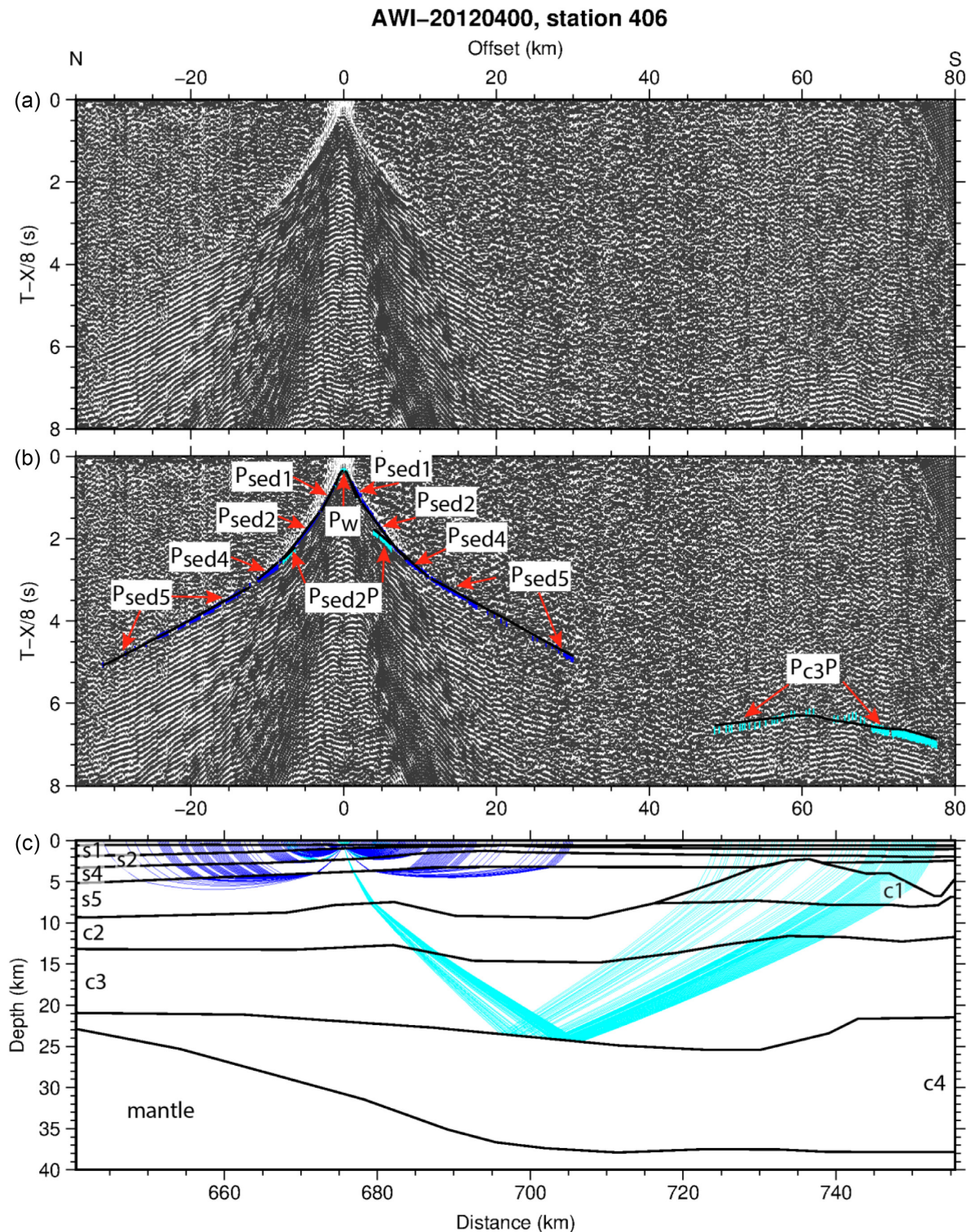
Figure 6. Picked and computed traveltimes of OBS 106. (a) Seismic record section of the hydrophone (h) component. (b) Same section, picked phases are shown in dark blue (refractions) and light blue (reflections). The computed traveltimes are shown as black lines, phase names are labelled. (c) Ray paths of the picked phases shown above. Black lines mark the layer boundaries of the velocity layers. Sedimentary layers (s1–s5), crustal layers (c2–c4) and the mantle are labelled.

dependent on the node distribution, since the resolution in the areas between nodes is always interpolated. Therefore, the good resolution of the upper mantle down to a depth of 25 km between km 250 and 450 can be explained by a large distance between velocity nodes

and is not the result of a good ray coverage in this area (Fig. 10d). Indeed, in the upper mantle, ray coverage is sparse and only present in the upper first kilometer of the mantle between km 300 and 400 (Fig. 12, lower left-hand panel).
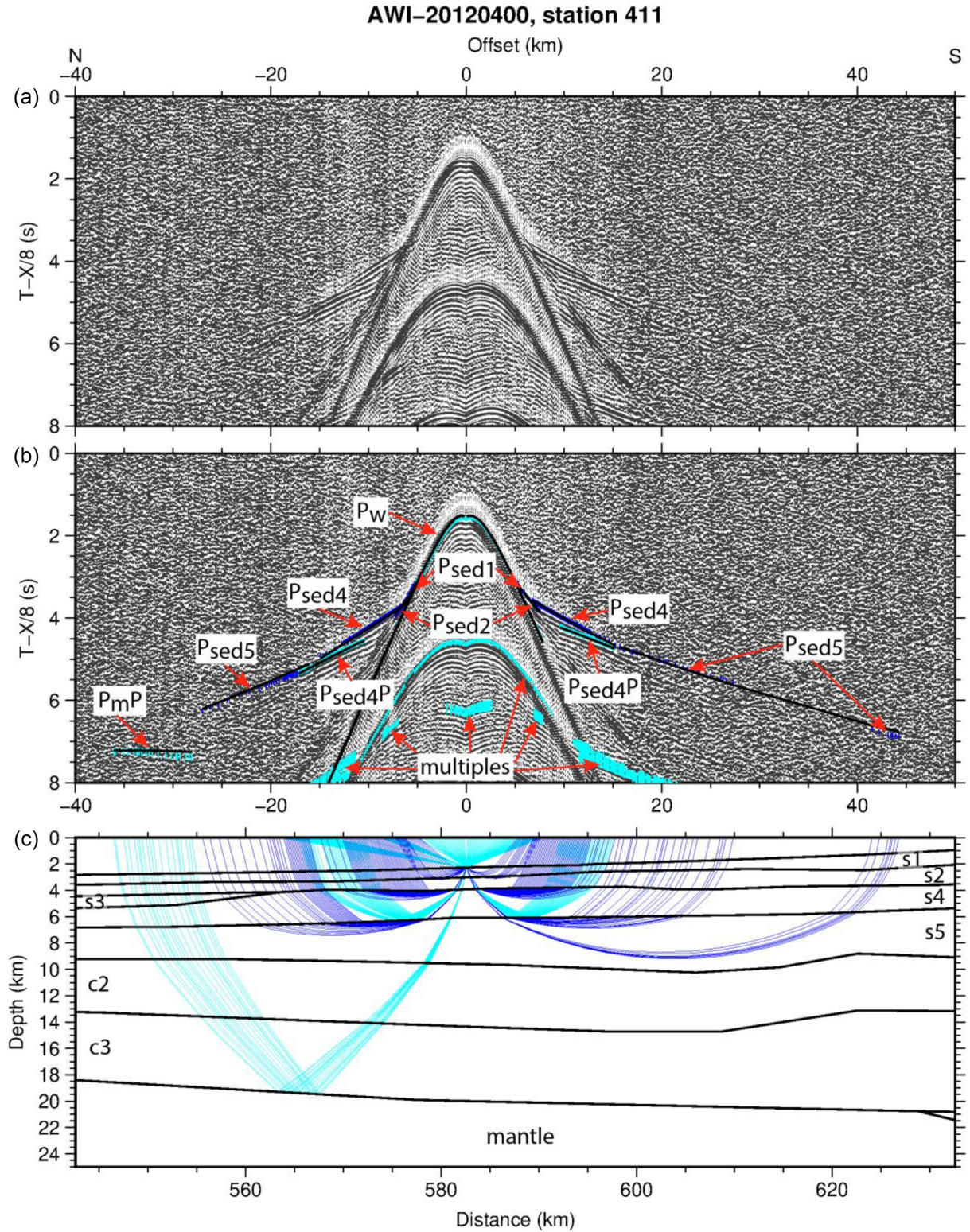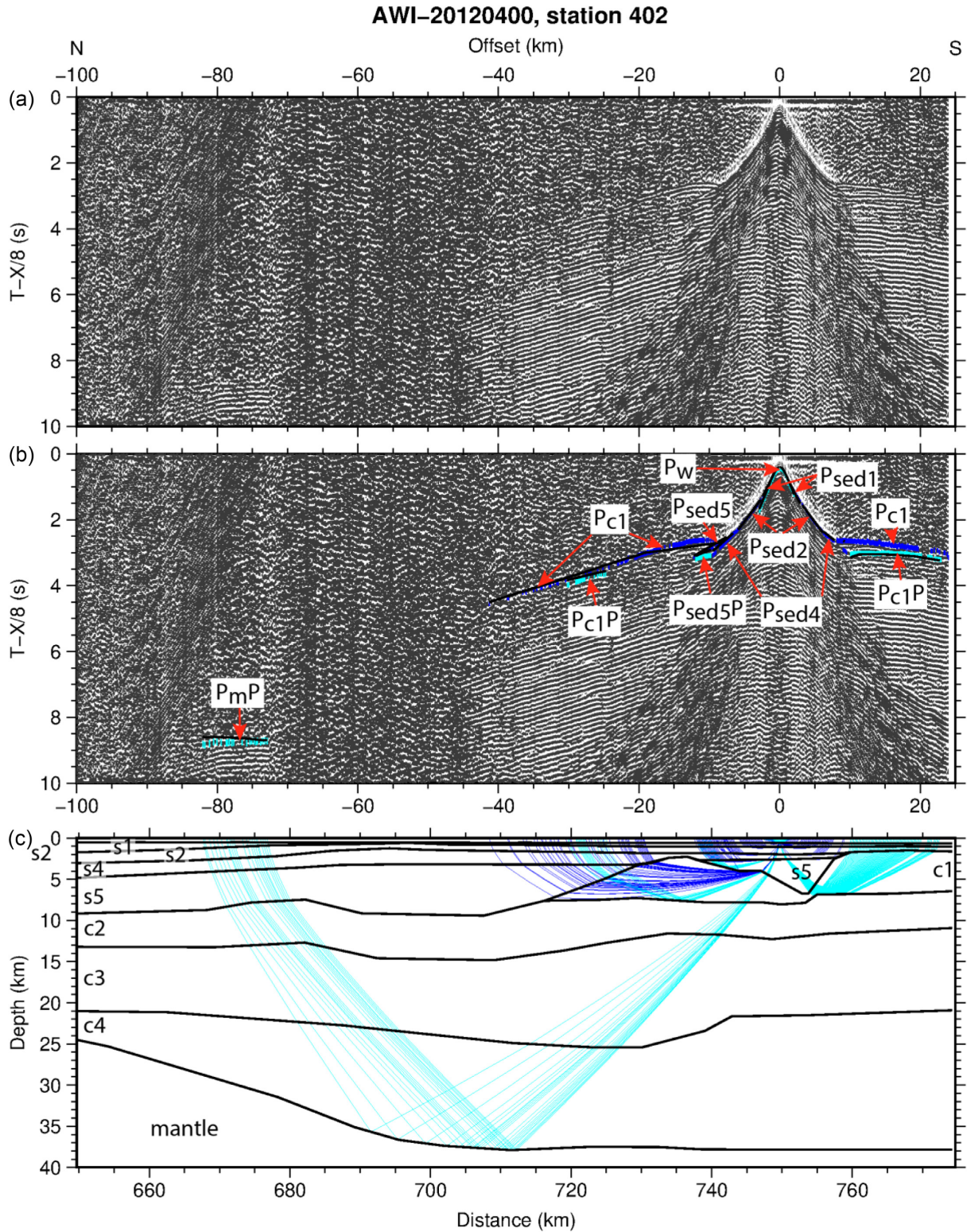
Figure 7. Picked and computed traveltimes of OBS 411. (a) Seismic record section of the hydrophone (h) component. (b) Same section, picked phases are shown in dark blue (refractions) and light blue (reflections). The computed traveltimes are shown as black lines, phase names are labelled. (c) Ray paths of the picked phases shown above. Black lines mark the layer boundaries of the velocity layers. Sedimentary layers (s1–s5), crustal layers (c2, c3) and the mantle are labelled.

Figure 8. Picked and computed traveltimes of OBS 406. (a) Seismic record section of the vertical (z) component. (b) Same section, picked phases are shown in dark blue (refractions) and light blue (reflections). The computed traveltimes are shown as black lines, phase names are labelled. (c) Ray paths of the picked phases shown above. Black lines mark the layer boundaries of the velocity layers. Sedimentary layers (s1–s2, s4–s5), crustal layers (c1–c4) and the mantle are labelled.

To estimate model uncertainties, the depths of layer boundaries and layer velocities were adjusted until the fit of the calculated traveltimes violated the estimated pick error range. The model seismic velocity uncertainties resulting from this procedure are ± 0.1 km s^{-1} for

sedimentary and upper crustal layers and increase up to ± 0.2 km s^{-1} for the lowermost crust and mantle. The depth uncertainties generally vary between ± 50 and ± 500 m for the base of sedimentary layers and ± 0.5 and ± 1 km for the base of crustal layers. The largest

Figure 9. Picked and computed traveltimes of OBS 402. (a) Seismic record section of the vertical (*z*) component. (b). Same section, picked phases are shown in dark blue (refractions) and light blue (reflections). The computed traveltimes are shown as black lines, phase names are labelled. (c) Ray paths of the picked phases shown above. Black lines mark the layer boundaries of the velocity layers. Sedimentary layers (s1–s2, s4–s5), crustal layers (c1–c4) and the mantle are labelled.
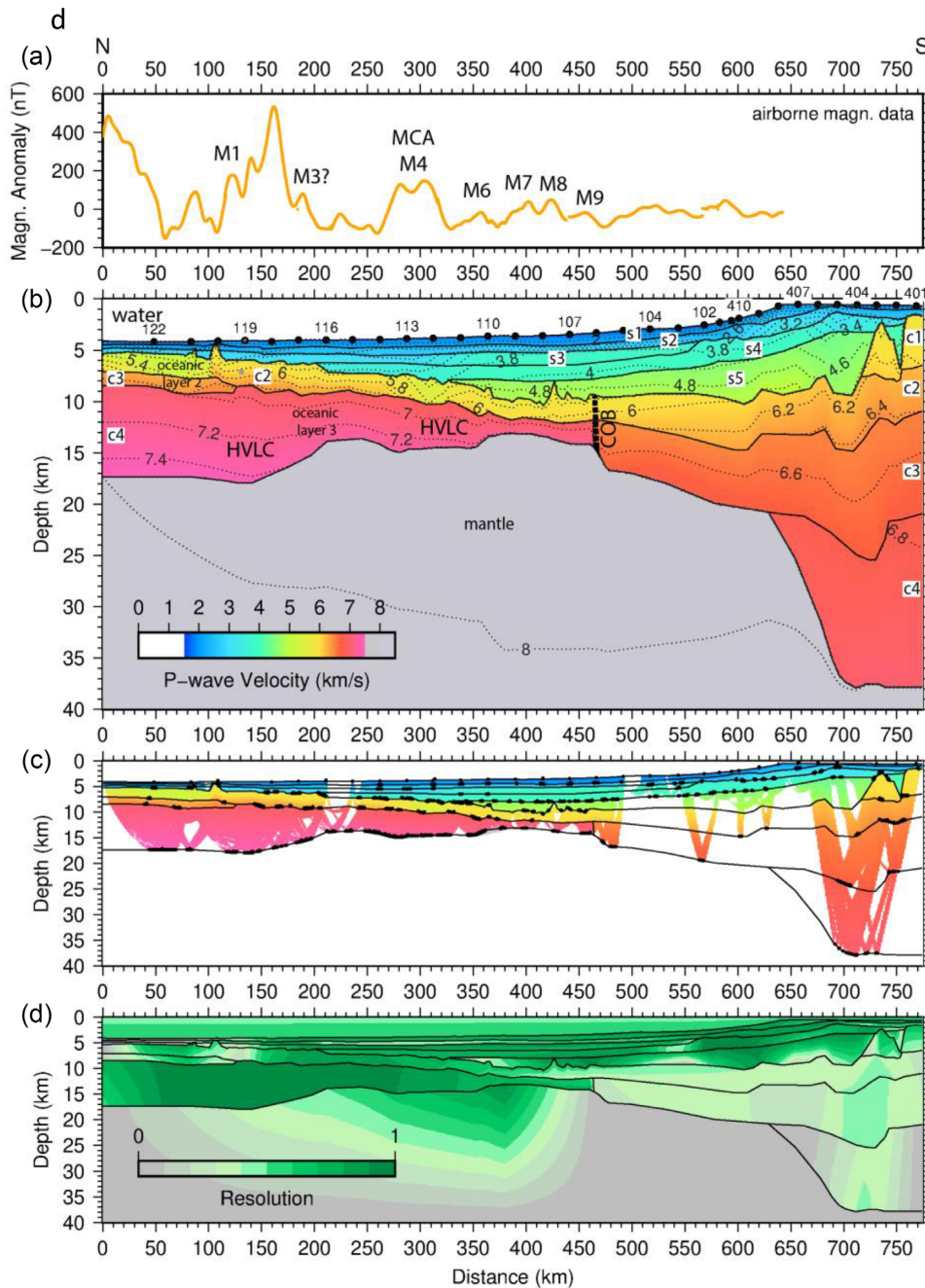
Figure 10. *P*-wave velocity model and helicopter borne magnetic data. (a) Observed magnetic data (orange) along our profile. Identified isochrons (partly taken from Jokat *et al.* 2021) are numbered. The location of the COB is taken from Jokat et al. (2021). (b) *P*-wave velocity model. Black circles mark the positions of OBS on the seafloor. OBS 119, which was lost, is coloured in grey. Numbers above the circles indicate the OBS number. Black lines mark the boundaries of the different velocity layers. Sedimentary layers (s1–s5) and crustal layers (c1–c4) are labelled. (c) Ray coverage of the *P*-wave velocity model shown in (b). Areas without ray coverage are coloured white. Layer boundaries verified by reflections are marked with a thick black line. (d) Resolution of the *P*-wave velocity model. Abbreviations: COB, continent–ocean boundary; HVLC, high velocity lower crust; MCA, Mac Robertson magnetic anomaly.

exception is for the Moho depth below the Prydz Bay shelf south of km 700, where uncertainty increases to ±3 km.

2.4 Gravity data

Gravity data were acquired coincident with the seismic lines. Along AWI-20070100, RV *Polarstern*'s gravity meter KSS-31 (Bodenseewerke) recorded continuously during the entire experiment.

A CHEKAN-AM marine gravimeter installed on RV *Karpinskiy* recorded gravity data along AWI-20120400. Processing of the gravity data consisted of the following steps: filtering of the raw data, a time shift of 235 s, correction of the Eötvös effect using the navigation data, connection of the harbour gravity value to IGSN71 world gravity net, and subtraction of the normal gravity (WGS85). The ISGN ties were achieved using measurements made with a LaCoste Romberg gravity meter (G-877) at stations in Punta Arenas (Chile),

20070100 & 20120400
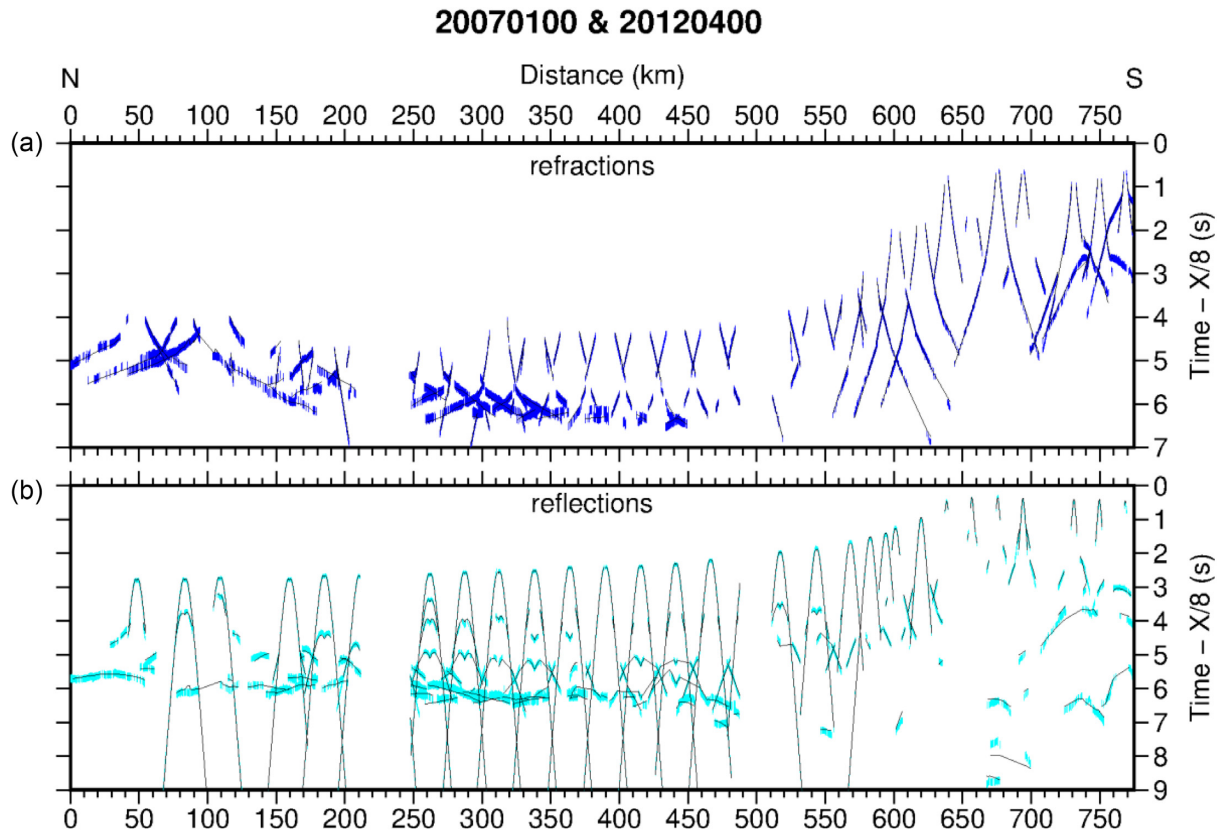
Figure 11. Picks and computed traveltimes (changed after Jokat *et al.* 2021). Black lines mark the computed traveltimes. Traveltime picks for refractions are dark blue, picks for reflections are light blue. The lengths of the picks represent the assigned uncertainties.

Davis Station (the Australian Antarctic station in Prydz Bay), Port-aux-Français and Drygalsky Station (Kerguelen Islands) and Cape Town (South Africa).

2.5 Density modelling

Free-air gravity anomalies along the profile range from −9 to +19 mGal in the oceanic crust (Fig. 13). A strong positive gravity anomaly appears over the Prydz Bay shelf from km 570 onwards, peaking at 103 mGal over the shelf edge.

To verify our *P*-wave velocity model, we used the software GM-SYS™ to generate a density model. The structure and layers of the *P*-wave velocity model were used as the starting point for the 2-D gravity modelling. The model was extended 800 km in each direction to minimize edge effects. For the start model (Fig. 13, red lines and numbers), boundaries of the velocity layers were taken as the boundaries of constant-density polygons. The average seismic velocities were converted to densities based on the velocity–density relationship of Ludwig *et al.* (1970). If the *P*-wave velocity within a layer changed significantly, the polygons were subdivided further and the subdivisions were assigned average density values.

The starting model produced large residuals (Fig. 13, red line) in the shelf/slope area. This is a well-known problem along rifted margins related to the contrasting thicknesses of oceanic and continental lithosphere (Breivik *et al.* 1999). The mantle was subdivided into 5 polygons with slightly varying densities (Fig. 13, model 1) to account for this. The result of this step was a significant improvement in the fit of the observed and calculated anomalies. Smaller

misfits of 10 mGal are present at both ends of the profile and between km 330 and 370. A large misfit occurs between calculated and observed gravity at km 620–700 over part of the shelf where sparse ray coverage of the entire crust leaves the velocity model poorly constrained (Fig. 12, km 500–680). A second density model (Fig. 13, model 2) with increased densities in parts of the continental crust reduced the misfit at the shelf break to a maximum of 20 mGal.

2.6 Magnetics

Helicopter magnetic data were collected with a Scintrex caesium vapor magnetometer during the expedition in 2007. The bird carrying the magnetometer was towed 30 m below a helicopter. Several lines were acquired parallel to the seismic profile (Fig. 1b), resulting in a 20–30 km wide swath centred on AWI-20070100. The data were processed using standard procedures, but without diurnal corrections since no base station data were available. Over the oceanic crust, the data show good correlations of magnetic anomalies between the dense flight lines. Jokat *et al.* (2021) interpreted these anomalies in terms of magnetic reversal isochrons.

3 RESULTS AND INTERPRETATION

The composite profile AWI-20070100 and AWI-20120400 depicts the crustal structure of the shelf off Prydz Bay (PB, East Antarctica) and the Enderby Basin (EB) to the north (Fig. 10). We briefly describe our results for the different segments of the line, directly followed by our interpretations of them.
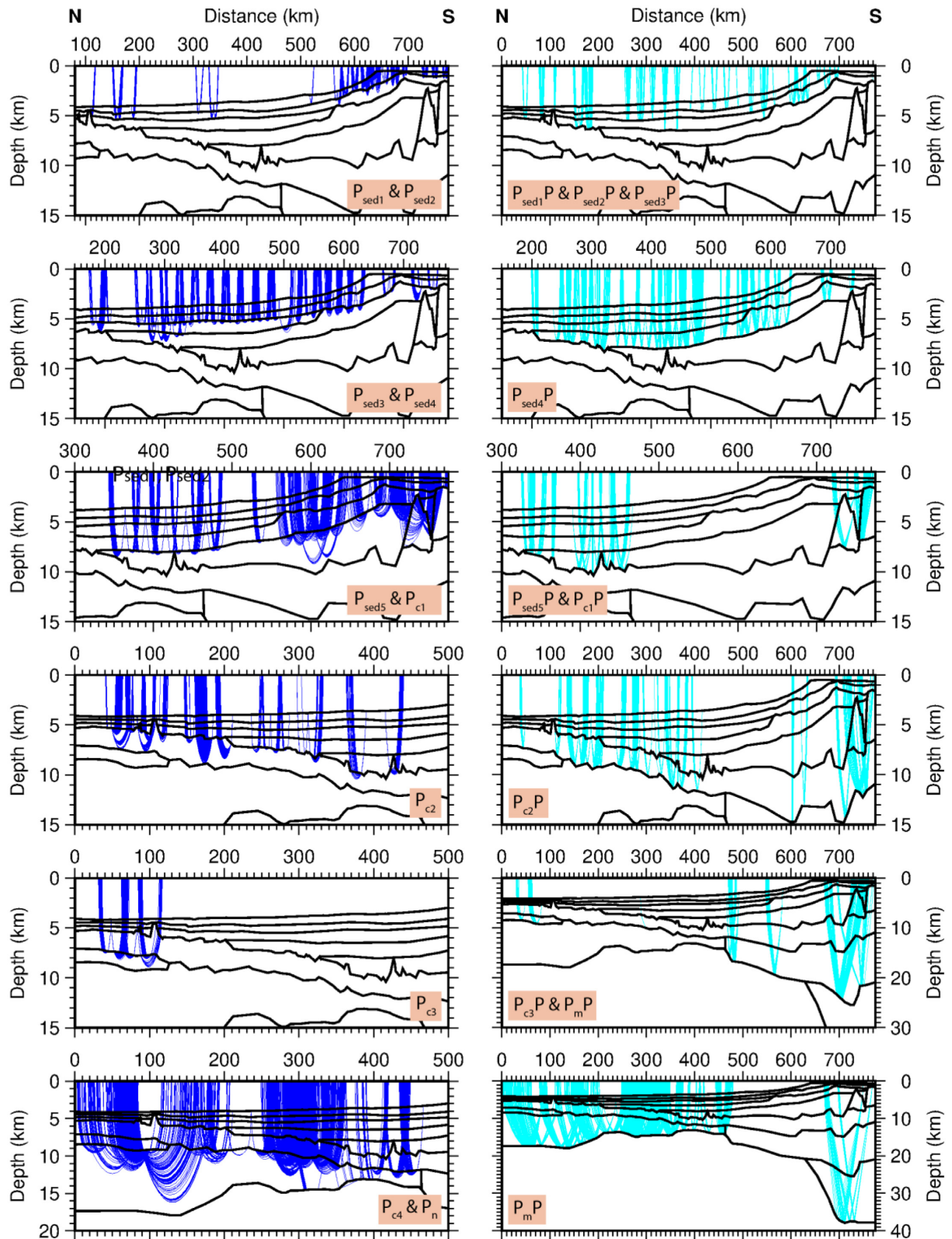
AWI–20070100 & 20120400

Figure 12. Ray coverage (changed after Jokat *et al.* 2021). Black lines mark the boundaries of different velocity layers. Refractions are marked in dark blue, reflected rays are coloured light blue. The corresponding phase names are displayed in each panel.

Table 1. Number of picks, tRMS, χ^2 and uncertainties for different velocity layers.

Phase	Number of picks	tRMS (s)	χ^2	Assigned pick uncertainties (s)
P_w	4559	0.045	0.979	0.045
P_{sed1}	181	0.046	0.834	0.050
$P_{sed1}P$	259	0.045	0.812	0.050
P_{sed2}	551	0.043	0.738	0.050
$P_{sed2}P$	399	0.077	1.642	0.060
P_{sed3}	873	0.041	0.479	0.060
$P_{sed3}P$	330	0.058	0.951	0.060
P_{sed4}	556	0.047	0.609	0.060
$P_{sed4}P$	1398	0.059	0.971	0.060
P_{sed5}	967	0.056	0.887	0.060
$P_{sed5}P$	367	0.086	1.504	0.070
P_{c1}	340	0.070	0.996	0.070
$P_{c1}P$	126	0.063	0.829	0.070
P_{c2}	693	0.065	0.667	0.080
$P_{c2}P$	756	0.072	0.817	0.080
P_{c3}	194	0.038	0.221	0.080
$P_{c3}P, P_mP$	343	0.088	0.969	0.090
P_{c4}	1618	0.051	0.324	0.090
P_mP	2012	0.079	0.619	0.100
P_n	71	0.067	0.450	0.100
All	16 593	0.059	0.808	-

The final velocity–depth model consists of eleven layers in total. Velocities in the five sedimentary layers (s1–s5, Fig. 10) increase from 1.7 km s^{-1} (s1) to 5.1 km s^{-1} (s5). The highest *P*-wave velocities modelled in the uppermost sedimentary layers (s1 and s2, 3.0 and 3.5 km s^{-1}) appear in the shelf area (Fig. 10). Layer s3 velocities are well constrained by refractions (P_{sed3}) in the central part of the model and range between 2.9 and 3.9 km s^{-1}. Layer s3 ranges in thickness from ∼1.5 km in the central part of the profile to less than 400 m in the north. The apparent pinch-out of s3 at km 565 is a technical, rather than geological, feature, since rayinvr does not allow two velocity layers to be combined into one. Layer s4 velocities (3.1–4.0 km s^{-1}) are well constrained by numerous refracted arrivals (P_{sed4}) in the shelf area, but fewer in the central part of the model. The layer s4 is up to 2.5 km thick. The thickness of the lowermost sedimentary layer, s5, decreases from a maximum of 6.3 km beneath the shelf area to zero in the deep sea. Its *P*-wave velocities range between 4.0 and 5.1 km s^{-1}. While the boundary between the sedimentary layers and basement is clearly visible in the seismic refraction and MCS data in the northern and central parts of the profile (Figs 3 and 12), it is only confirmed by a handful of reflections within the graben structure at the southernmost end of profile AWI-20120400 (Figs 2 and 12).

The crystalline crust is modelled with up to four layers (c1–c4, Fig. 10). The total crustal thickness varies greatly, from ∼3.5 km in the central part of the profile, to 36.5 km at its southern end. We subdivide the crust into continental, transitional and oceanic domains along the profile, based on its velocity distribution, layer thicknesses and observational constraints from the coincident seismic reflection lines.

3.1 Transitional and continental crust (km 470–774)

The uppermost crystalline crustal layer c1, with a thickness of up to 5.2 km, is limited to the southern end of the model (Fig. 10, km 720–774). *P*-wave velocities in c1 range between 5.7 and 6.1 km s^{-1} and might be related to synrift, sediment-filled half grabens partly

imaged by the MCS data on the shelf (Fig. 2). Outside of this range, the underlying layer, c2, represents the uppermost acoustic basement. Its thickness strongly varies between ∼3.5 and ∼5 km (Fig. 10). Because of the lack of refracted arrivals, velocities of 5.8–6.3 km s^{-1} in the upper parts of c2 and 6.1–6.5 km s^{-1} near its base were calculated based on reflected arrivals only. The mid crystalline crustal layer, c3 (Fig. 10, km 465–774), has a rather homogenous *P*-wave velocity distribution of 6.5–6.8 km s^{-1} and its thickness varies between 4 and 11 km. The lowermost crust below the shelf area (c4) was modelled with *P*-wave velocities of 6.8–7.0 km s^{-1} resulting in a maximum thickness of 17 km. The total crystalline crustal thickness below the Prydz Bay shelf sums to 36 km. We found no evidence for magmatic underplating, which would be characterized by seismic velocities above 7.0 km s^{-1}, in this segment. Increased densities in the crystalline crust between km 620 and 690 (2.93 g cm^{-3}, Fig. 13) could be an indication for mafic rocks and intrusions in this part of the profile.

We compare five velocity–depth profiles taken between kms 500 and 750 to representative profiles for extended continental and average continental crust worldwide (Figs 14b and c). The crustal velocity profiles south of km 650 match profiles for extended and average continental crust (Figs 14b and c, red profiles). The velocity distribution, velocity gradients and thickness of the crust seawards, between km 500 and 650, differ from the typical ranges for continental or oceanic crust (Figs 14c, d and e, orange profiles). Consequently, we interpret this part of the profile to image the continent–ocean transition (COT).

Following Whitmarsh & Miles (1995), the COT can be defined as the region between thinned continental crust, which is typically characterized by tilted fault blocks, and the first occurrence of linear magnetic reversal anomalies formed by seafloor spreading. The seaward termination of the COT is at km 470, where the first seafloor spreading anomalies were identified (Jokat *et al.* 2021). We place the southern limit of the COT at km 700, where we see a significant shallowing of the Moho and tilted fault blocks below the continental shelf. Thus, the minimum width of the COT in the Prydz Bay region is 230 km.

3.2 Oceanic crust (km 0–470)

An abrupt step-like southwards rise in the Moho, from ∼16.5 to ∼14 km depth, occurs between OBS 105 and 106 (Fig. 10, km 460–480), close to the southernmost, oldest, magnetic seafloor spreading anomalies (Jokat *et al.* 2021). The step marks a relatively sharp northwards increase in crustal *P*-wave velocities in the lowermost crustal layer. It is well constrained by reflections (Fig. 6). Northwards, numerous refracted phases constrain the crustal velocities and their gradients (Fig. 12), as well as the Moho, all the way to km 0. The ray coverage constraining the velocity distribution within the different crystalline crustal layers is good to excellent. It generally reveals the presence of two layers, a typical feature of normal oceanic crust worldwide, except between km 0 and ∼128 where we can distinguish another, ∼1.5-km-thick crustal layer (c3, Fig. 10). *P*-wave velocities in all these layers lie in typical ranges for oceanic crust worldwide (Figs 14d–f). Like Jokat *et al.* (2021), we interpret the step at km 470 to mark the COB, or onset of oceanic crust, which continues northwards to the end of the profile at km 0.

For a more detailed interpretation, Figs 14(d) and (e) compare velocity–depth functions taken every 50 km between km 50 and 600 to global compilations of oceanic crust. Between km 250 and 450, velocity gradients and the thickness of the crust are within the
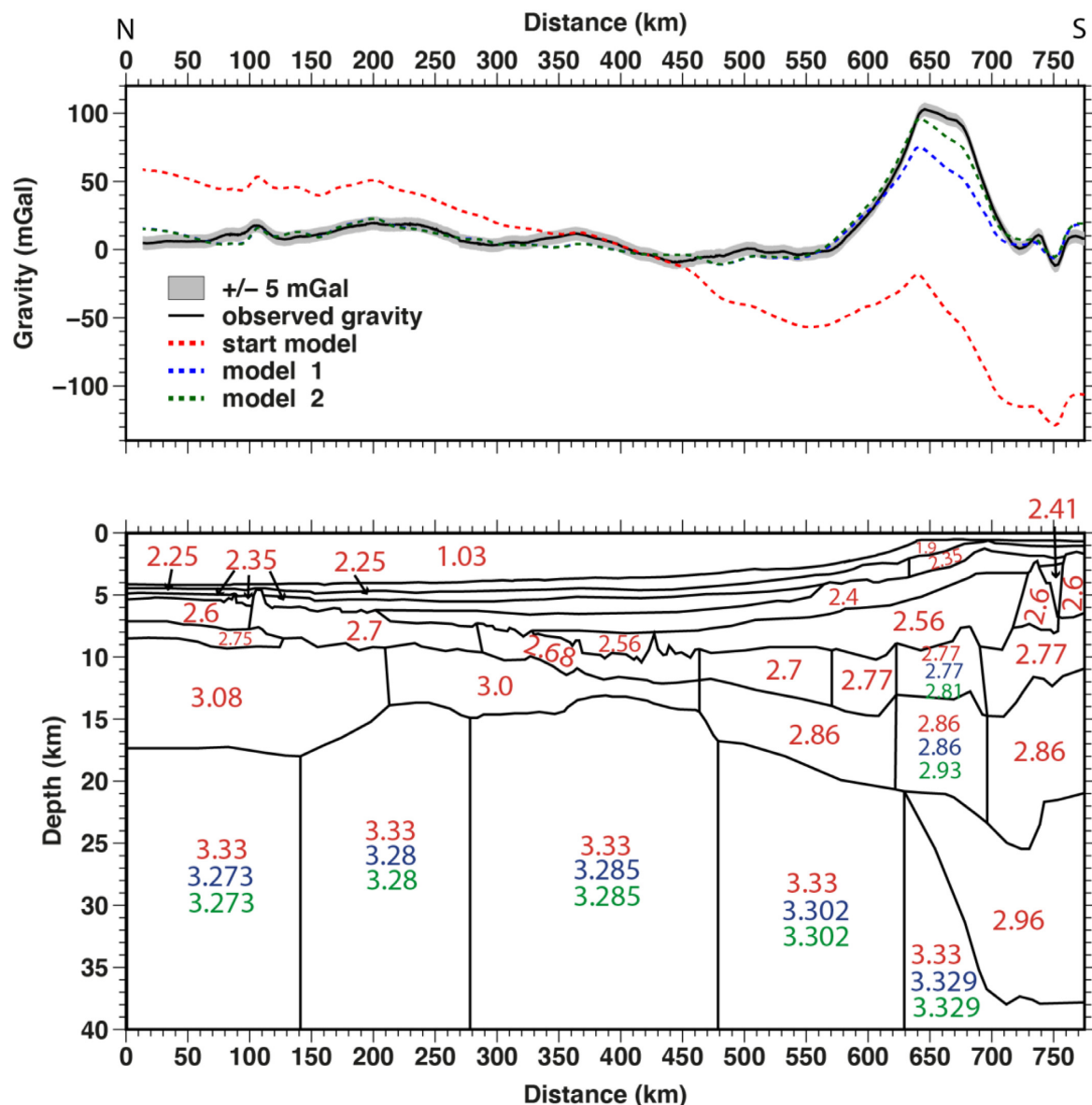
Figure 13. Density model. The upper panel shows the observed (black) and calculated (red, blue, and green) free-air anomalies. The lower panel shows the density model derived from our *P*-wave velocity model. Density values are given in g cm^{-3}. Red numbers indicate the densities used in the starting model. Where the density values used for model 1 (blue numbers) and our final model 2 (green numbers) differ from the ones used for the start model, they are written below the red values.

range of Atlantic and Pacific oceanic crust (White *et al.* 1992). We also compared velocity–depth functions to the newest global compilation of oceanic crust by Christeson *et al.* (2019), who grouped velocity–depth functions based on spreading rates (slow to intermediate spreading and fast to superfast spreading) and age of the oceanic crust (younger or older than 7.5 Ma). Spreading rates for the up to 133 Ma year old oceanic crust along our model range from slow to superfast (20–220 mm yr^{-1}, Jokat *et al.* 2021). In our model, velocities in oceanic layer 3 are higher than in the compilation of Christeson *et al.* (2019), while velocities and thickness of oceanic layer 2 are within the range of typical oceanic crust, However, high velocities are not uncommon in the region. The thinnest (∼3.5–5 km) parts of our oceanic crust, at km 350–450, resemble the 4.5–7-km-thick oceanic crust observed in the Indian Ocean south of Sri Lanka (Altenbernd *et al.* 2020, Fig. 14f). The

velocities and gradients at km 50, 100, 150 and 200 match very well with Indian Ocean oceanic crust (Fig. 14f). North of km 350, the oceanic crust significantly thickens towards the end of the line on the southern rim of the Kerguelen Plateau by which point the crust is considerably thicker (up to 13 km in total) than the global average for oceanic crust (6.15 km; Christeson *et al.* 2019). Here, *P*-wave velocities increase to 7.0 km s^{-1} at the top and 7.5 km s^{-1} at the base of c4, the lower crustal layer 2. Velocities in this range are not typical of normal oceanic lower crust, but diagnostic of the so-called high-velocity lower crustal (HVLC) layers commonly observed in oceanic LIPs (e.g. Coffin & Eldholm 1994; Ridley & Richards 2010; Hochmuth *et al.* 2014). The velocity–depth functions and thickness of the lowermost crustal layer north of km 200 also match well with the oceanic crustal structure in the Enderby Basin along line 7 (Charvis & Operto 1999, Fig. 14f).
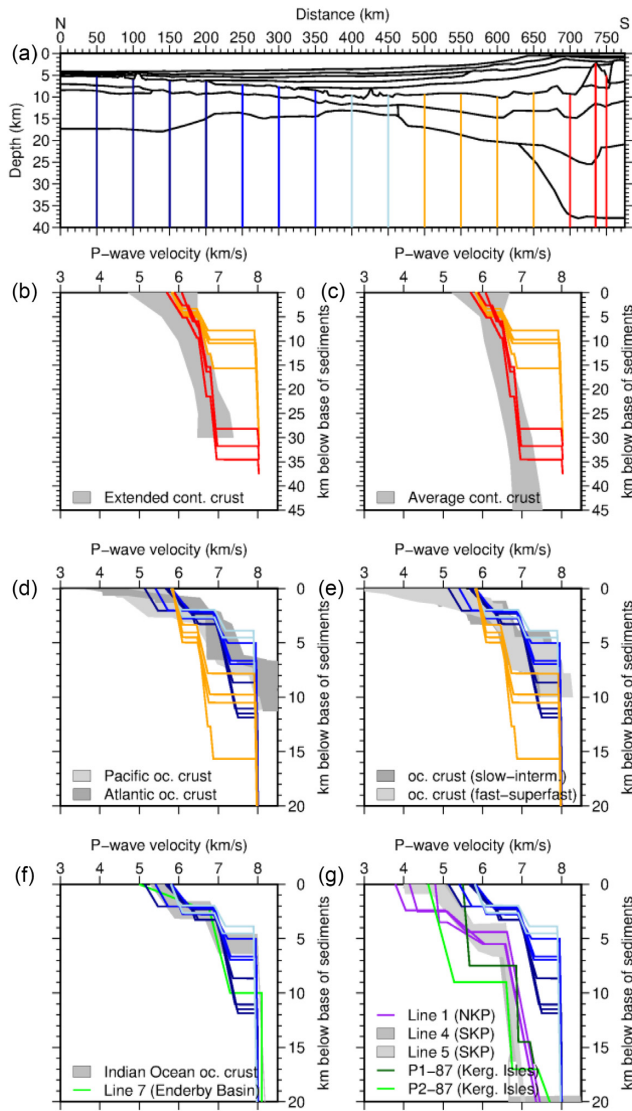
Figure 14. Comparison of velocity–depth profiles along our profile with results of other crustal studies. (a) Positions of the velocity depth profiles taken along our model are indicated by coloured lines. (b) Comparison of velocity–depth profiles taken between km 500–750 with profiles on extended continental crust (Christensen & Mooney 1995). (c) Comparison of velocity–depth profiles taken between km 500 and 750 with profiles on average continental crust (Christensen & Mooney 1995). (d) Comparison of velocity–depth profiles taken between km 50 and 450 with profiles on 59–127 Ma old Atlantic and 29–140 Ma old Pacific oceanic crust (White *et al.* 1992). (e) Comparison of velocity–depth profiles taken between km 50 and 450 with profiles on >7.5 Ma old oceanic crust generated at slow to intermediate and fast to superfast spreading rates (Christeson *et al.* 2019). (f) Comparison of velocity–depth profiles taken between km 50 and 350 with profiles on Indian Ocean oceanic crust (Altenbernd *et al.* 2020) and on line 7 (Charvis & Operto 1999) in the Enderby Basin. (g) Comparison of velocity–depth profiles taken between km 50 and 350 with profiles on the lines 1, P1-87 and P2-87 (Charvis *et al.* 1995), and profiles located on line 4 and line 5 at the SKP (Operto & Charvis 1995, 1996).

4 DISCUSSION

Estimated locations for the onset of oceanic crust along rifted margins, the COB, are widely used as constraints in plate kinematic reconstructions. The most reliable estimates can be made using a combination of wide-angle and magnetic data, which show the distributions of relatively high crustal velocities and magnetic reversal anomalies that are characteristic of most oceanic crust. Previous studies in the Enderby Basin, in the absence of wide-angle data, proposed a wide range of contrasting COB locations based on seismic reflection, magnetic and gravity data (Figs 1c and d). While the first studies (Powell *et al.* 1988; Ishihara *et al.* 1999) proposed a COB close to the present-day shelf break, later ones (Gaina *et al.* 2003; Stagg *et al.* 2004; Gaina *et al.* 2007) shifted it much farther north (400 km) to a position near 65°S over the abyssal plain. These interpretations relied on interpretations of gravity, magnetic and seismic reflection data and imply the presence of an extremely wide COT off Prydz Bay (Gaina *et al.* 2007).

Here, we merge several geophysical data sets to provide an enhanced estimate for the distribution of oceanic crust in the Enderby Basin. To do this, we interpret a previously-published compilation of magnetic data (Golynsky *et al.* 2018) together with observational insights from several Russian and Australian MCS profiles (Fig. 15) to extrapolate the COB and newly published identifications of magnetic reversal isochrons (Jokat *et al.* 2021) into the Enderby Basin westwards (Fig. 16) of our deep seismic line.

First, we describe some previous interpretations of the basin's geophysical characteristics in greater detail. Stagg *et al.* (2004) used magnetic, gravity and seismic reflection and refraction data to locate the COB in our area of interest. Their COB correlates with an oceanward step-up in the basement of 500–1000 m (Fig. 15d). This step is in wide parts marked by a pronounced magnetic anomaly, the Mac Robertson Coast Anomaly (MCA, Fig. 16). The MCA is a strong linear positive magnetic anomaly that runs continuously across the Enderby Basin from east to west. Using magnetic and MCS data, Gaina *et al.* (2007) also interpreted the MCA to mark the COB (Fig. 16). Beginning north of this prominent anomaly, they identified conjugate sets of seafloor spreading isochrons in a sequence starting with *M*9 (Fig. 1) flanking an extinct spreading centre marked by either isochron *M*2 or *M*0. Gibbons *et al.* (2013) proposed alterations to this scheme, keeping an extinct ridge crest in a similar location, but suggesting a younger age for it in an attempt to account for the results of a dense aeromagnetic survey close to Gunnerus Ridge forming the western boundary of the Enderby Basin at ∼33°E (Jokat *et al.* 2010). The extinct ridge exists in both schemes because of the interpretation of microcontinents beneath Elan Bank and the SKP, which requires a two-phase model to separate them first from Antarctica and later from India by a northward jump of the Indian–Antarctic Plate boundary.

Both Gaina *et al.*'s (2007) and Gibbons *et al.*'s (2013) sets of conjugate isochron identifications were made with variable-vintage data collected near and over the southern flank of the KP. However, there is a strong possibility that the magnetic anomalies represent the products of shallow eruptions responsible for the formation of the large igneous province rather than a record of geomagnetic polarity reversals in oceanic crust. The distribution of continental and oceanic crust in those studies thus mainly relied on the interpretation of low-quality and/or noisy magnetic data. Magnetic data south of the MCA in particular showed only weak anomalies and were difficult to interpret, such that deep seismic data were required to test Gaina *et al.*'s (2007) idea of the MCA as representing the COB/onset of seafloor spreading in the Enderby Basin.

A recent study (Jokat *et al.* 2021) provided the necessary deep seismic profile, AWI-20070100/AWI-20120400, and used it as part of an extensive study of the Enderby Basin to challenge the two-phase model. As shown in Fig. 10, it is clear that the MCA (*M*4)
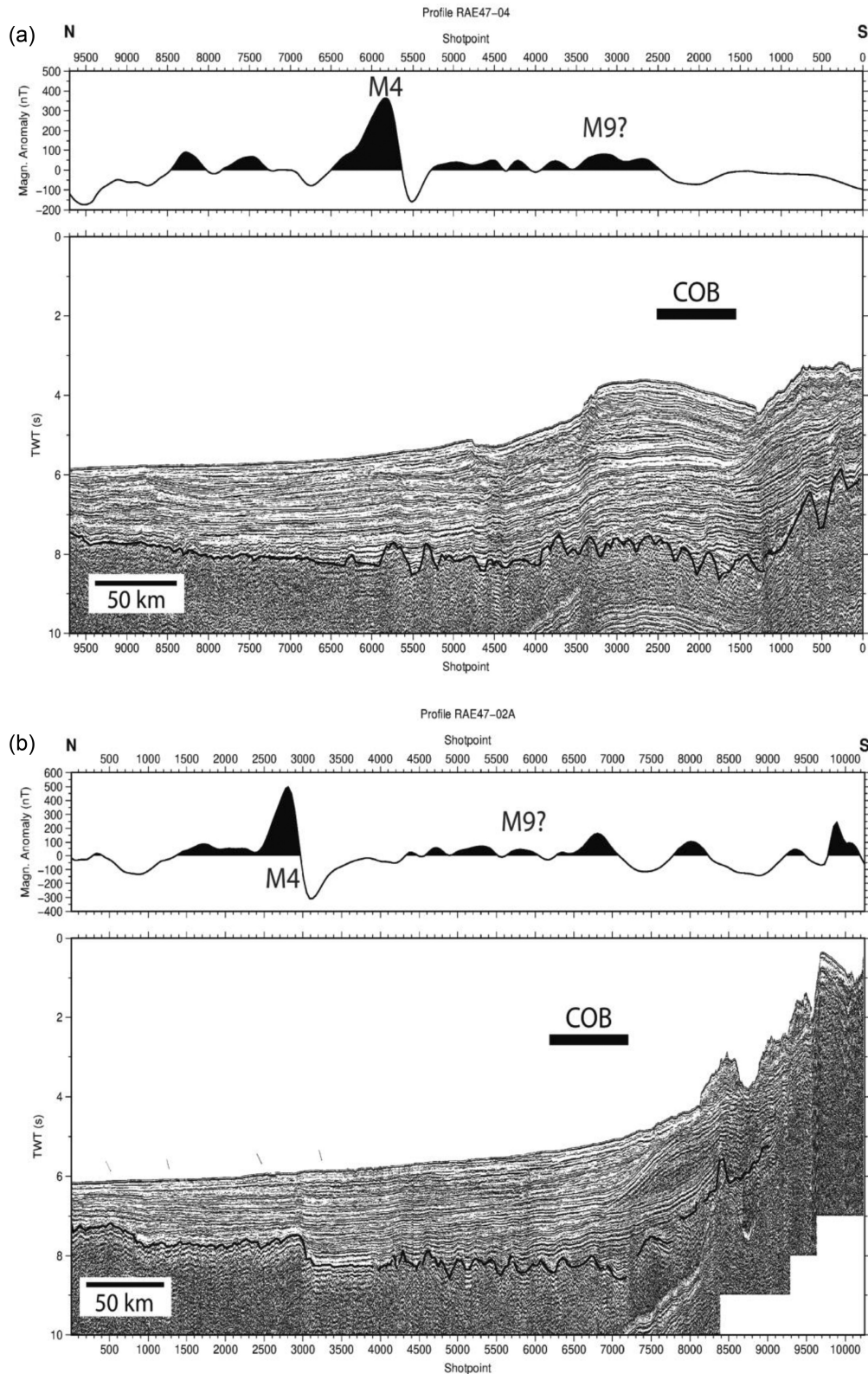
Figure 15. (a)–(d) Seismic reflection and magnetic data along Russian and Australian profiles. Locations of the profiles are shown in Fig. 16. The MCS profiles show the basement variations in the area where the onset of oceanic crust is proposed. Two critical magnetic chrons picked from the ADMAP grid (Golynsky *et al.* 2018) as well as the area of the COB are labelled as done for the other seismic reflection lines. However, we do not consider its location as reliable. Chron *M*4 is the most prominent magnetic anomaly in the Enderby Basin, which in older studies was interpreted as COB (Stagg *et al.* 2004; Gaina *et al.* 2007; Gibbons *et al.* 2013). (d) Only along this line the COB of Stagg *et al.* (2004) does not coincide with the position of *M*4 and is labelled. White numbers within the basement are sonobuoy velocities in km s⁻¹ (Stagg *et al.* 2004). Since our seismic refraction profile is parallel to the Australian profile GA229-30 (Fig. 16), the yellow numbers indicate the velocities we have determined in the same region along our profile.
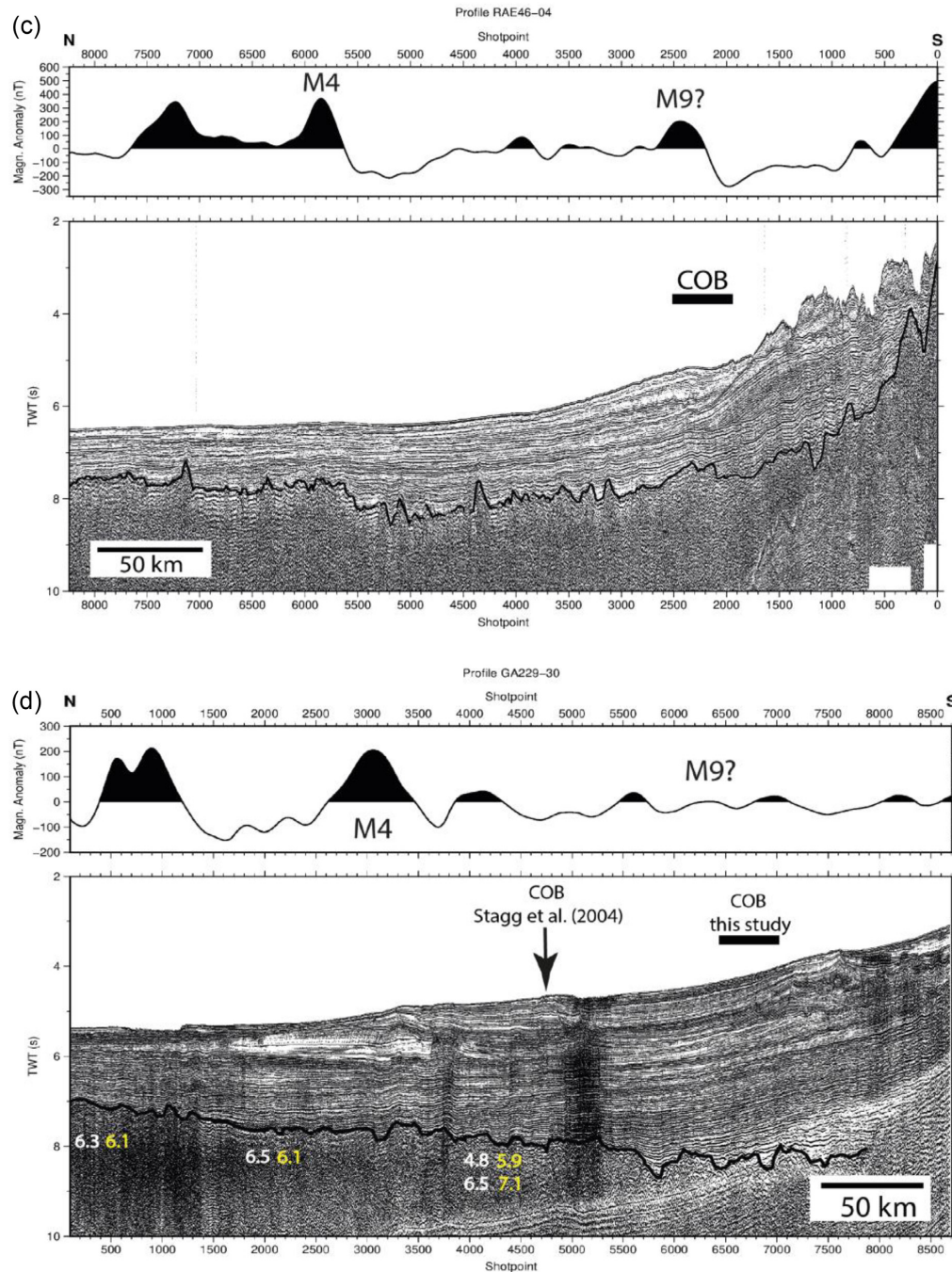
Figure 15. Continued

does not mark the COB, but instead expresses part of the basin's oceanic crustal floor. Jokat *et al.* (2021) used dense helicopter-borne magnetic data (Figs 1 and 16) acquired along and parallel to the profile to interpret the MCA as the prominent magnetic reversal isochron *M*4, which lies ∼160 km north of the COB (Figs 10 and 16). Between the new COB and *M*4, they interpreted a weakly developed sequence of magnetic seafloor spreading anomalies starting with M9r (133 Ma) north of the seismically defined COB. The M-series anomaly sequence continues north of the MCA/*M*4 with *M*3 and *M*1 over the SKP. Neither the magnetic nor the seismic data provided any evidence for the presence of an extinct spreading axis (Jokat *et al.* 2021).

We extrapolate Jokat *et al.*'s (2021) new magnetic isochron identifications around line AWI-20070100/AWI-20120400 into the wider Enderby Basin (Fig. 16) using ADMAP2, the most recent Antarctic magnetic data compilation (Golynsky *et al.* 2018). The randomly oriented magnetic data of the ADMAP2 grid do not resolve the low amplitude anomalies south of MCA/*M*4 well on their own, but can be picked using the helicopter magnetic data as a starting reference. As a result, Fig. 16 shows isochron *M*9 running parallel to and south of chron *M*4, into the region west of the profile. North of MCA/*M*4, the ADMAP2 grid is very noisy, perhaps owing to complex volcanic and intrusive structures near the southern edge of the Kerguelen Plateau. Based on this, we consider any isochron
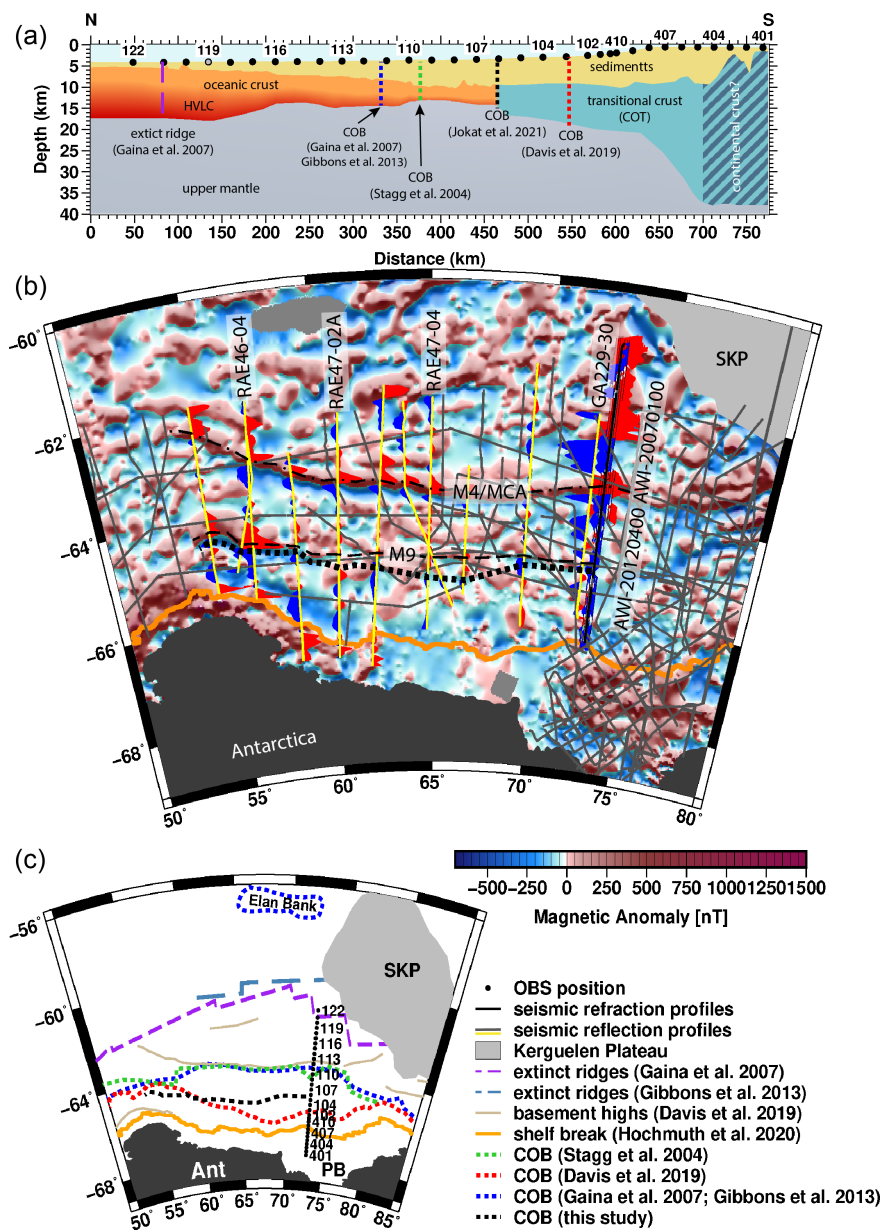
Figure 16. Interpretation. (a) Geological interpretation of our profile. The proposed COB positions/extinct spreading ridge of other authors are marked. (b) Magnetic anomalies (Golynsky *et al.* 2018) in the Enderby Basin and Prydz Bay region. Grey and yellow solid lines show the positions of Australian (Stagg *et al.* 2004) and Russian MCS data (Gandyukhin *et al.* 2002; Leitchenkov *et al.* 2015; Antarctic Seismic Data Library System SDLS). The dashed line marks the location of the magnetic chrons *M*4/MCA and *M*9. The *M*4/MCA is identical with the picks of Gaina *et al.* (2007). Blue and red wiggles at 72°E are dense helicopter borne magnetic data acquired in a corridor around the seismic refraction profiles AWI20120400/AWI-20070100. The yellow seismic lines are underlain by magnetic wiggles extracted from the ADMAP grid (Golynsky *et al.* 2018). (c) Comparison of the position of our COB with the COBs proposed by other authors. Abbreviations: Ant, Antarctica; COB, continent ocean boundary; COT, continent–ocean transition; HVLC, high-velocity lower crust; MCA, Mac Robertson magnetic anomaly; PB, Prydz Bay; SKP, Southern Kerguelen Plateau.

identifications close to the edge of the KP (over and north of the northern part of our seismic line) as highly questionable.

To test our tentative extrapolation of isochrons *M*9 and *M*4, we plotted our magnetic picks together with Russian and Australian MCS data acquired during the RAE-40, RAE-46, RAE-47 GA228 and GA229 expeditions (Gandyukhin *et al.* 2002; Stagg *et al.* 2004; Leitchenkov *et al.* 2015, Fig. 15). This reveals two interesting correlations.

First, chron *M*9, which lies immediately north of the COB on the deep seismic profile, often coincides in the MCS data

with locations where acoustic basement ceases to dip seawards and becomes horizontal (Figs 15a and b). Similar observations are reported from the African–Antarctic spreading sector (Mueller & Jokat 2019) and especially from the East Greenland margin (Voss & Jokat 2007), where strong Cenozoic seafloor spreading anomalies correlate well with the above described basement geometry. An exception can be observed on line 4604 (Fig. 15c), where the basement continues to dip seawards across *M*9 to the north of the proposed COB. An explanation for this observation is not immediately apparent but could be related to its location at the boundary/edge of two

different spreading systems (Jokat *et al.* 2021). Another exception can be observed on line GA229-30 (Fig. 15d), where the basement reflector south of shotpoint 7500 is not easy to identify.

Second, starting around isochron *M*4 (130 Ma) the oceanic basement continuously shallows northwards towards the edge of the Kerguelen Plateau on four profiles (Figs 3 and 15). In a 'normal' oceanic deep abyssal plain we would expect that the oceanic basement remains more or less at the same depth level. While continental crust generally exhibits velocities less than 7.0 km s^{-1}, the influence of a hotspot can lead to intense intrusions into existing crust or the formation of new entirely igneous crust with velocities well above 7.0 km s^{-1} (e.g. 90° East Ridge (Grevemeyer *et al.* 2001), the Walvis Ridge (Fromm *et al.* 2015) or the Manihiki Plateau (Hochmuth *et al.* 2014)). Similar velocities are encountered along our profile, together with the thickening of its oceanic layer 3 to form the so-called HVLC that starts around km 360. Jokat *et al.* (2021) attribute the shallowing of the oceanic basement and thickening of the oceanic crust to the arrival and influence of the Kerguelen plume.

In 2001 and 2002, Australian institutions acquired deep seismic, gravity, and magnetic data in our research area. One of these seismic reflection profiles, line GA229-30, is located parallel to our seismic refraction profile (Fig. 16). Because our profile is so close and parallel to the GA profile, we can easily compare our crustal velocities and the position of our COB with the findings of Stagg *et al.* (2004).

Since the basement reflector at the southern end of profile GA229-30 is not visible, the typical basement geometry we identified on various lines in the region (Figs 15a and b) could not be used to locate the COB. Therefore, we have extrapolated the COB from our seismic refraction profile to line GA229-30. Notably, our determined COB is located farther south than those of Stagg *et al.* (2004). Stagg *et al.* (2004) also determined crustal velocity profiles based on sonobuoy data for different parts of the profile (Fig. 15d, white numbers). Yellow numbers indicate corresponding average velocities determined along our profile. In comparison, our measured and modelled velocities of the upper oceanic layers are lower than the ones modelled by Stagg *et al.* (2004). In the middle of the profile GA229-30 (SP4200), the difference is largest (4.8 km s^{-1} versus 5.9 km s^{-1}). However, it is notable that a velocity of 4.8 km s^{-1} was also measured along our profile, but in the sediments covering the oceanic crust (Fig. 10b, layer s5). Nevertheless, the velocity differences are quite high. One explanation might be that, in contrast to our velocity model, the sonobuoy data were modelled with fixed interval velocities (Stagg *et al.* 2004), and not, like in our model, with velocity gradients. Also, data from a OBSs located on the seafloor are usually much more accurate and of better quality than data from sonobuoys that drift in the water.

How do our findings compare with results of other regional deep seismic profiles? While the thickness and velocities of the oceanic layer 2 (Fig. 10) along our profile are typical for oceanic crust, velocities of up to 7.5 km s^{-1} in the HVLC are significantly higher than reported from the lower crust of lines 4 and 5 at the SKP (Raggatt Basin) farther east (Operto & Charvis 1996) or line 6 at Elan Bank (Borissova *et al.* 2003, Figs 1 and 14g). Operto & Charvis (1995, 1996) interpreted the crustal structure of the Raggatt Basin along lines 4 and 5 as stretched continental crust overlain by basalt flows. Along both lines, the maximum velocity of the lower crust is 6.9–7.0 km s^{-1}. At line 4, a reflective lower crust with average velocities of 6.7 km s^{-1} is observed. Additionally, the crust is much thicker (up to 22 km) than along our profile (Fig. 14g). As in the Raggatt Basin (lines 4 and 5), no HVLC was identified below the

Elan Bank on line 6 (Fig. 1), where the lowermost part of the up-to 17 km-thick crust is characterized by velocities of around 6.6 km s^{-1}, revealing a crustal structure similar to that of the Raggatt Basin at the SKP (Borissova *et al.* 2003). A ∼40-km-wide high velocity body (∼7.0 km s^{-1}) in the eastern part of line 6 is interpreted by Borissova *et al.* (2003) as a high-density plutonic body caused by extensive magmatism. While the crustal structure identified along our transect partly differs from these more northern parts of the SKP, it is in close agreement with that reported from the NKP, where HVLC layers have been reported (e.g. line 1, Figs 1 and 14g, Charvis *et al.* 1995). Along line 1, the lower crust is twice as thick as in our profile, with velocities ranging between 6.5 and 7.5 km s^{-1}. Another HVLC has been identified below the Kerguelen archipelago, where a 2.5-km-thick layer with velocities of 7.2–7.5 km s^{-1} is described as marking a transition zone between the crust and mantle, underlying a 3–7-km-thick oceanic layer 3 with velocities of 6.65–6.9 km s^{-1} (e.g. Recq *et al.* 1990; Charvis *et al.* 1995). Differences in the crustal thickness and velocity distribution, as depicted in Fig. 14(g), show the heterogeneity of the crustal structure of the KP, which is probably related to differences in the magmatic activity of the Kerguelen hotspot through time.

Our joint interpretation of deep seismic sounding data and dense magnetic data shows that the initial breakup that occurred around magnetic chron M9r (km 470, Fig. 10) was followed by the formation of thin oceanic crust. Hence, breakup occurred in a magma poor environment, suggesting that the Kerguelen mantle plume was either not generating voluminous melts at 133 Ma, or its melt was not being transported to the Enderby Basin off Prydz Bay. The former interpretation is supported by the absence of large amounts of volcanic material onshore Antarctica and India at that time. The first availability of more significant melt dates to around chron M6n times, with the first appearance of normal thickness (∼7 km) oceanic crust on our profile (km 360 to km 200, Fig. 10). Unusually-high (>7 km s^{-1}) seismic velocities in the lower part of this oceanic crust indicates the presence of a HVLC, which can be attributed to a plume origin for the melt. Towards the north, a further increase in crustal and HVLC thickness is encountered at km 200 (Fig. 10). Here the oceanic crust is approx. 128 Myr old (chron M3n; Jokat *et al.* 2021). In addition, our density model (Fig. 13) shows that the density of the upper mantle decreases towards the SKP. This can be an effect of low-density material, derived from the Kerguelen plume, in the upper mantle. Therefore, the mantle and crustal structure revealed along our profile have been influenced by a long period of increasing activity related to the early phase of the Kerguelen hotspot.

5 CONCLUSION

Interpretation of our *P*-wave velocity profile reveals details of the crustal structure off Prydz Bay. Extended continental crust is identifiable south of km 670. The COT along our profile is at least 230 km wide with the onset of oceanic crust located at ∼km 470. While the oceanic crust north of the COB is initially very thin, at only 3.5 km, it thickens northwards of km 360 and with increasing proximity to the SKP.

During the first phase of seafloor spreading, thin oceanic crust was formed between chrons *M*9 and *M*7 in a magma-poor regime. During chrons *M*6 and *M*4, the magma supplies increased due to the onset of the Kerguelen mantle plume's influence. As a consequence, thickened oceanic crust containing a HVLC was formed.

Based on newly compiled magnetic data, we were able to extrapolate magnetic chron identifications (chrons *M*9 and *M*4) south of chron *M*4 into the region west of our deep seismic line. Seismic reflection data show correlatable basement features that can be understood to support this extrapolation. Specifically, we interpret the area where the general basement topography becomes horizontal to be indicative of the COB. A shallowing of the oceanic basement further north around chron *M*4 is interpreted to be caused by extra melt delivered by the strengthening Kerguelen mantle plume. These results allow a tighter fit of India and Antarctica and dismiss a two-phase opening model for both plates.

AUTHOR CONTRIBUTION STATEMENT

TAL: data processing, data analysis, writing (original draft), visualization. WJ: Funding acquisition, magnetic data analysis, project administration, writing (review and editing). GL: writing (review and editing).

DATA AVAILABILITY

Wide-angle seismic data will be made available via www.pangaea.de by the end of the year 2022. Before, they are available from the corresponding author upon request. The Russian and Australian data are available via the SCAR Antarctic Seismic Data Library System for Cooperative Research (SDLS, https://www.scar.org/resources/seismic-data/).

REFERENCES

Altenbernd, T., Jokat, W. & Geissler, W., 2020. The bent prolongation of the 85°E Ridge south of 5°N – fact or fiction?, *Tectonophysics,* **785,** 228457, doi:10.1016/j.tecto.2020.228457.

Banerjee, B., Sengupta, B.J. & Banerjee, P.K., 1995. Signals of Barremian (116 Ma) or younger oceanic crust beneath the Bay of Bengal along 14°N latitude between 81°E and 93°E, *Mar. Geol.,* **128,** 17–23.

Borissova, I., Coffin, M.F., Charvis, P. & Operto, S., 2003. Structure and development of a microcontinent: Elan Bank in the southern Indian Ocean, *Geochem. Geophys. Geosyst.,* **4**(9), doi:10.1029/2003GC000535.

Breivik, A.J., Verhoef, J. & Faleide, J.I., 1999. Effect of thermal contrasts on gravity modeling at passive margins: results from the western Barents Sea, *J. geophys. Res.,* **104,** 15 293–15 311.

Charvis, P. & Operto, S., 1999. Structure of the Cretaceous Kerguelen Volcanic Province (southern Indian Ocean) from wide-angle seismic data, *J. Geodyn.,* **28,** 51–71.

Charvis, P., Recq, M., Operto, S. & Brefort, D., 1995. Deep structure of the northern Kerguelen Plateau and hotspot-related activity, *Geophys. J. Int.,* **122,** 899–924.

Christensen, N.I. & Mooney, W.D., 1995. Seismic velocity structure and composition of the continental crust: a global view, *J. geophys. Res.,* **100,** 9761–9788.

Christeson, G.L., Goff, J.A. & Reece, R.S., 2019. Synthesis of oceanic crustal structure from two-dimensional seismic profiles, *Rev. Geophys.,* **57,** 504–529.

M. F.Coffin, M. S.Pringle R. A.Duncan T. P.Gladczenko M.Storey R. D.Müller & L. A.Gahagan 2002. Kerguelen Hotspot Magma Output since 130 Ma, *J. Petrol.,* **43** 1121–1137.),

Coffin, M.F. & Eldholm, O., 1994. Large igneous provinces: crustal structure, dimensions, and external consequences, *Rev. Geophys.,* **32**(1), 1–36.

Davis, J.K., Lawver, L.A., Norton, I.O., Dalziel, I.W.D. & Gahagan, L.M., 2019. The crustal structure of the Enderby Basin, East Antarctica, *Mar. geophys. Res.,* **40,** 1–16.

Desa, M., Ramana, M. V. & Ramprasad, T., 2006. Seafloor spreading magnetic anomalies south off Sri Lanka, *Mar. Geol.,* **229,** 227–240.

Eagles, G., Pérez-Díaz, L. & Scarselli, N., 2015. Getting over continent ocean boundaries, *Earth Sci. Rev.,* **151,** 244–265

Frey, F.A. *et al.*, 2000. Origin and evolution of a submarine large igneous province: the Kerguelen Plateau and Broken Ridge, southern Indian Ocean, *Earth planet. Sci. Lett.,* **176,** 73–89.

Frey, F.A., Coffin, M.F., Wallace, P.J. & Weis, D., 2003. Leg 183 Synthesis: kerguelen Plateau-broken ridge-a large igneous province, *Proc. Ocean Drill. Prog., Sci. Results,* **183,** 1–48.

Frey, F.A., Weis, D., Borisova, A.Y.U. & Xu, G., 2002. Involvement of continental crust in the formation of the Cretaceous Kerguelen Plateau: new perspectives from ODP Leg 120 Sites, *J. Petrol.,* **43,** 1207–1239.

Fromm, T., 2016. PRay—a graphical user interface for interactive visualization and modification of rayinvr models, *J. appl. Geophys.,* **124,** 1–3.

Fromm, T., Planert, L., Jokat, W., Ryberg, T., Behrmann, J.H., Weber, M.H. & Haberland, C., 2015. South Atlantic opening: a plume-induced breakup?, *Geology,* **43**(10), 931–934.

Gaina, C., Müller, R.D., Brown, B. & Ishihara, T., 2003. Microcontinent formation around Australia, *Geol. Soc. Aust. Spec. Publ.,* **22,** 399–410.

Gaina, C., Müller, R.D., Brown, B., Ishihara, T. & Ivanov, S., 2007. Breakup and early seafloor spreading between India and Antarctica, *Geophys. J. Int.,* **170,** 151–169.

Gandyukhin, V., Gouseva, Y, Kudryavtsev, G., Ivanov, S. & Leitchenkov, G., 2002. Crustal structure, seismic stratigraphy and tectonic history of the Cosmonaut Sea sedimentary basin (Antarctica, southern Indian Ocean), *Explor. Protect. Miner. Resour.,* **9,** 27–31, in Russian, abstract and figure captions in English.

GEBCO Compilation Group, 2021. *GEBCO 2021 Grid*. doi:10.5285/c6612cbe-50b3-0cff-e053-6c86abc09f8f.

Gibbons, A.D., Whittaker, J.M. & Müller, R.D., 2013. The breakup of East Gondwana: assimilating constraints from Cretaceous ocean basins around India into a best-fit tectonic model, *J. geophys. Res.,* **118,** 808–822.

Golynsky, A. V. *et al.*, 2018. New magnetic anomaly map of the Antarctic, *Geophys. Res. Lett.,* **45,** 6437–6449.

Grevemeyer, I., Flueh, E.R., Reichert, C., Bialas, J., Kläschen, D. & Kopp, C., 2001. Crustal architecture and deep structure of the Ninetyeast Ridge hotspot trail from active-source ocean bottom seismology, *Geophys. J. Int.,* **144,** 414–431.

Hochmuth, K., Gohl, K., Leitchenkov, G., Sauermilch, I., Whittaker, J.M., Uenzelmann-Neben, G., Davy, B. & De Santis, L., 2020. The evolving Paleobathymetry of the Circum-Antarctic Southern Ocean Since 34 Ma: a key to understanding past Cryosphere-Ocean developments, *Geochem., Geophys. Geosyst.,* **21**(8), doi:10.1029/2020GC009122.

Hochmuth, K., Gohl, K. & Werner, R., 2014. The diverse crustal structure and magmatic evolution of the Manihiki Plateau, central Pacific 1863–1905, *Solid Earth Discuss.,* **6**(2), 1863–1905.

Hubberten, H.W., 2008. The expedition Antarktis-XXIII/9 of the research vessel "Polarstern" in 2007, *Rep. Polar Mar. Res.,* **583,** 167.

Ingle, S., Weis, D. & Frey, F.A., 2002. Indian continental crust recovered from Elan Bank, Kerguelen Plateau (ODP Leg 183, Site 1137), *J. Petrol.,* **43,** 1241–1257.

Ishihara, T., Leitchenkov, G.L., Golynsky, A. V., Alyavdin, S. & O'Brien, P.E., 1999. Compilation of shipborne magnetic and gravity data images crustal structure of Prydz Bay (East Antarctica), *Ann. di Geofis.,* **42,** doi:10.4401/ag-3716.

Jiang, Q., Jourdan, F., Olierook, H.K.H., Merle, R.E. & Whittaker, J.M., 2021. Longest continuously erupting large igneous province driven by plume-ridge interaction, *Geology,* **49,** 206–210.

Jokat, W., Altenbernd, T., Eagles, G. & Geissler, W.H., 2021. The early drift of the Indian plate, *Sci. Rep.,* **11,** doi:10.1038/s41598-021-90172-z.

Jokat, W., Boebel, T., König, M. & Meyer, U., 2003. Timing and geometry of early Gondwana breakup, *J. geophys. Res.,* **108**(B9), doi:10.1029/2002JB001802.

Jokat, W., Nogi, Y. & Leinweber, V., 2010. New aeromagnetic data from the western Enderby Basin and consequences for Antarctic-India break-up, *Geophys. Res. Lett.,* **37,** 1–5.

Kent, R.W., Pringle, M.S., Müller, R.D., Saunders, A.D. & Naresh, C.G., 2002. 40Ar/39Ar Geochronology of the Rajmahal Basalts, India, and their Relationship to the Kerguelen Plateau, *J. Petrol.,* **43,** 1141–1153.

König, M. & Jokat, W., 2010. Advanced insights into magmatism and volcanism of the Mozambique Ridge and Mozambique Basin in the view of new potential field data, *Geophys. J. Int.,* **180,** 158–180.

Leinweber, V.T. & Jokat, W., 2012. The Jurassic history of the Africa-Antarctica corridor—new constraints from magnetic data on the conjugate continental margins, *Tectonophysics,* **530-531,** 87–101.

Leitchenkov, G.L., Guseva, Y.B., Gandyukhin, V.V. & Ivanov, S.V., 2015. *Crustal Structure, Tectonic Evolution and Seismic Stratigraphy of the Southern Indian Ocean,* VNIIOkeangeologia. 200pp., in Russian, abstract and figure captions in English.

Ludwig, J., Nafe, J. & Drake, C., 1970. Seismic refraction, in *The Sea,* pp. 53–84, ed. Maxwell, A.E., Wiley-Interscience.

Lutter, W.J. & Nowack, R.L., 1990. Inversion for crustal structure using reflections from the PASSCAL Ouachita experiment, *J. geophys. Res.,* **95,** 4633–4646.

Mahoney, J.J., Jones, W.B., Frey, F.A., Salters, V.J.M., Pyle, D.G. & Davies, H.L., 1995. Geochemical characteristics of lavas from Broken Ridge, the Naturaliste Plateau and southernmost Kerguelen Plateau: cretaceous plateau volcanism in the southeast Indian Ocean, *Chem. Geol.,* **120,** 315–345.

Mahoney, J.J., Macdougall, J.D., Lugmair, G.W. & Gopalan, K., 1983. Kerguelen hotspot source for Rajmahal Traps and Ninetyeast Ridge?, *Nature,* **303,** 385–389.

Mueller, C.O. & Jokat, W., 2019. The initial Gondwana break-up: a synthesis based on new potential field data of the Africa-Antarctica Corridor, *Tectonophysics,* **750,** 301–328.

Nogi, Y., Seama, N., Isezaki, N. & Fukuda, Y., 1996. Magnetic anomaly lineations and fracture zones deduced from vector magnetic anomalies in the West Enderby Basin, *Geol. Soc. Spec. Publ.,* **108,** 265–273.

Operto, S. & Charvis, P., 1995. Kerguelen Plateau: a volcanic passive margin fragment?, *Geology,* **23,** 137–140.

Operto, S. & Charvis, P., 1996. Deep structure of the southern Kerguelen Plateau (southern Indian Ocean) from ocean bottom seismometer wide-angle seismic data, *J. geophys. Res.,* **101,** 25 077–25 103.

Powell, C.M.A., Roots, S.R. & Veevers, J.J., 1988. Pre-breakup continental extension in East Gondwanaland and the early opening of the eastern Indian Ocean, *Tectonophysics,* **155,** 261–283.

Ramana, M. V, Ramprasad, T. & Desa, M., 2001. Sea floor spreading magnetic anomalies in the Enderby Basin, East Antarctica, *Earth planet. Sci. Lett.,* **191,** 241–255.

Ramana, M. V. *et al.*, 1994. Mesozoic anomalies in the Bay of Bengal, *Earth planet. Sci. Lett.,* **121,** 469–475.

Recq, M., Brefort, D., Malod, J. & Veinante, J.L., 1990. The Kerguelen Isles (southern Indian Ocean): new results on deep structure from refraction profiles, *Tectonophysics,* **182,** 227–248.

Ridley, V.A. & Richards, M.A., 2010. Deep crustal structure beneath large igneous provinces and the petrologic evolution of flood basalts, *Geochem. Geophys. Geosyst.,* **11,** 1–21.

Royer, J. & Coffin, M., 1992. Jurassic to Eocene Plate tectonic reconstructions in the Kerguelen Plateau Region 1, in *Proceedings of the Ocean Drilling Program, Scientific Results,* Vol.**120,** pp. 917–928, eds Wise, S.W., Jr., Julson, A.P., Schlich, R. & Thomas, E. (Eds.), Texas A & M University Ocean Drilling Program.

Stagg, H.M.J., Colwell, J.B., Direen, N.G., O'Brien, P.E., Bernardel, G., Borissova, I., Brown, B.J. & Ishirara, T., 2004. Geology of the continental margin of Enderby and Mac Robertson Lands, East Antarctica: insights from a regional data set, *Mar. Geophys. Res.,* **25,** 183–219.

Sushchevskaya, N.M., Belyatsky, B. V., Tkacheva, D.A., Leitchenkov, G.L., Kuzmin, D. V. & Zhilkina, A. V., 2018. Early Cretaceous Alkaline Magmatism of East Antarctica: peculiarities, conditions of formation, and relationship with the Kerguelen Plume, *Geochem. Int.*, **56,** 1051–1070.

Talwani, M., Desa, M.A., Ismaiel, M. & Sree Krishna, K., 2016. The Tectonic origin of the Bay of Bengal and Bangladesh, *J. geophys. Res.,* **121,** 4836–4851.

Voss, M. & Jokat, W., 2007. Continent-ocean transition and voluminous magmatic underplating derived from P-wave velocity modelling of the East Greenland continental margin, *Geophys. J. Int.,* **170,** 580–604.

Weis, D., Ingle, S., Damasceno, D., Frey, F.A., Nicolaysen, K. & Barling, J., 2001. Origin of continental components in Indian ocean basalts: evidence from Elan Bank (Kerguelen Plateau, ODP Leg 183, site 1137), *Geology,* **29,** 147–150.

Wessel, P., Smith, W.H.F., Scharroo, R., Luis, J.F. & Wobbe, F., 2013. Generic mapping tools : improved version released, *EOS, Trans. Am. geophys. Un.,* **94,** 409–410.

White, R.S., McKenzie, D. & O'Nions, R.K., 1992. Oceanic crustal thickness from seismic measurements and rare earth element inversions, *J. geophys. Res.,* **97,** 19683.

Whitmarsh, R.B. & Miles, P.R., 1995. Models of the development of the west Iberia rifted continental margin at 40°30′N deduced from surface and deep-tow magnetic anomalies, *J. geophys. Res.,* **100,** 3789–3806.

Zelt, C.A. & Smith, R.B., 1992. Seismic traveltime inversion for 2-D crustal velocity structure, *Geophys. J. Int.,* **108,** 16–34.